

**Thermische Wechselbeanspruchung von
Absorberbeschichtungen unter konzentrierter
Solarstrahlung**

**Thermal Cycling of Solar Absorber Coatings under
Concentrated Solar Flux**

Masterarbeit von
Marcos Esteller Vela
IRS-18-S-034

Betreuer:
Prof. Dr. Stefanos Fasoulas
Dr.-Ing. Stefan Löhle
Universität Stuttgart, Institut für Raumfahrtsysteme (IRS)
Dipl.-Ing. Simon Caron
Deutsches Zentrum für Luft- und Raumfahrt e.V. (DLR)
Institut für Solarforschung, Almeria, Spanien

Institut für Raumfahrtsysteme
Universität Stuttgart

Pfaffenwaldring 29
70569 Stuttgart

April 2018



Master Thesis Work
of Mr. Marcos Estellar Vela

Thermische Wechselbeanspruchung von Absorberschichten unter konzentrierter Solarstrahlung
Thermal cycling of solar absorber coatings under concentrated solar flux

Motivation:

New high temperature solar absorber coatings are being developed within the European project RAISELIFE. These coatings are designed with a high solar absorptance in order to improve the efficiency of steam and molten salt tower receivers. A set of steel substrates and coatings have to be tested under realistic conditions to understand their failure mechanisms and prove their durability. A parabolic dish testing facility has been upgraded at the Plataforma Solar de Almería in order to perform thermal cycles on tubular absorber samples under concentrated solar flux profiles. The focus of the work lies on performing accelerated aging tests, generate experimental data and improve test procedures.

Task description of the Master thesis work:

- Perform thermal cycles at the dish testing facility on coated samples
 - Measure solar absorptance according to a defined test protocol
 - Image the observed degradation using optical microscopy
- Improve the dish test bench between measurement campaigns
 - Compare measured and simulated flux densities
 - Integrate a water cooled radiometer
 - Adapt control strategy algorithm
- Collect and analyze experimental data
 - Quality check for thermal cycles and flux profiles
 - Evolution of solar absorptance before and after exposure
- Comparison of degradation with accelerated ageing tests in climate chambers
 - Ranking the different coatings regarding the expected service life time
- Documentation

The thesis will be accomplished at DLR Institute for Solar Research, Plataforma Solar de Almeria (Spain).

Internal supervisor: Dr.-Ing. Stefan Löhle

External supervisor: Dipl.-Ing. Simon Caron

Starting date: 01.02.2017

Submission until: 31.07.2017

Acknowledgement of receipt:

I hereby confirm that I read and understood the task of the master thesis, the juridical regulations as well as the study- and exam regulations.

Prof. Dr.-Ing. Stefanos Fasoulas
(Responsible Professor)

External Supervisor

Signature of the student

Legal Restrictions: The Editor/s is/are principally not entitled to make any work and research results which he/she receives in process, accessible to third parties without the permission of the supervisor. Already achieved research results respect the Law on Copyright and related rights (Federal Law Gazette I / S. 1273, Copyright Protection Act of 09.09.1965). The Editor has the right to publish his/her findings unless no findings and benefits of the supervising institutions and companies have been incorporated. The rules issued by the branch of study for making the bachelor thesis and the exam regulations must be considered.

IRS Professors and Associate Professors:

Prof. Dr.-Ing. Stefanos Fasoulas (Managing Director) · Prof. Dr.-Ing. Sabine Klinkner (Deputy Director) ·
Prof. Dr. rer. nat. Alfred Krabbe · (Deputy Director) · Hon.-Prof. Dr.-Ing. Jens Eickhoff · Prof. Dr. rer. nat. Reinhold Ewald ·
PD Dr.-Ing. Georg Herdrich · Hon.-Prof. Dr. Volker Liebig · Prof. Dr.-Ing. Stefan Schleichriem · PD Dr.-Ing. Ralf Srama

Erklärungen

Hiermit versichere ich, Esteller Vela, Marcos, dass ich diese Masterarbeit selbstständig mit Unterstützung des Betreuers / der Betreuer angefertigt und keine anderen als die angegebenen Quellen und Hilfsmittel verwendet habe. Die Arbeit oder wesentliche Bestandteile davon sind weder an dieser noch an einer anderen Bildungseinrichtung bereits zur Erlangung eines Abschlusses eingereicht worden. Ich erkläre weiterhin, bei der Erstellung der Arbeit die einschlägigen Bestimmungen zum Urheberschutz fremder Beiträge entsprechend den Regeln guter wissenschaftlicher Praxis¹ eingehalten zu haben. Soweit meine Arbeit fremde Beiträge (z.B. Bilder, Zeichnungen, Textpassagen etc.) enthält, habe ich diese Beiträge als solche gekennzeichnet (Zitat, Quellenangabe) und eventuell erforderlich gewordene Zustimmungen der Urheber zur Nutzung dieser Beiträge in meiner Arbeit eingeholt. Mir ist bekannt, dass ich im Falle einer schuldhaften Verletzung dieser Pflichten die daraus entstehenden Konsequenzen zu tragen habe.



.....
Almeria, 30.04.2018,

Hiermit erkläre ich mich damit einverstanden, dass meine Masterarbeit zum Thema: *Thermische Wechselbeanspruchung von Absorberbeschichtungen unter konzentrierter Solarstrahlung*

in der Institutsbibliothek des Instituts für Raumfahrtssysteme Masterarbeit öffentlich zugänglich aufbewahrt und die Arbeit auf der Institutswebseite sowie im Online-Katalog der Universitätsbibliothek erfasst wird. Letzteres bedeutet eine dauerhafte, weltweite Sichtbarkeit der bibliographischen Daten der Arbeit (Titel, Autor, Erscheinungsjahr, etc.). Nach Abschluss der Arbeit werde ich zu diesem Zweck meinem Betreuer neben dem Prüfexemplar eine weitere gedruckte sowie eine digitale Fassung übergeben.

Der Universität Stuttgart übertrage ich das Eigentum an diesen zusätzlichen Fassungen und räume dem Institut für Raumfahrtssysteme an dieser Arbeit und an den im Rahmen dieser Arbeit von mir erzeugten Arbeitsergebnissen ein kostenloses, zeitlich und örtlich unbeschränktes, einfaches Nutzungsrecht für Zwecke der Forschung und der Lehre ein. Falls in Zusammenhang mit der Arbeit Nutzungsrechtsvereinbarungen des Instituts mit Dritten bestehen, gelten diese Vereinbarungen auch für die im Rahmen dieser Arbeit entstandenen Arbeitsergebnisse.



.....
Almeria, 30.04.2018,

¹ Nachzulesen in den DFG-Empfehlungen zur „Sicherung guter wissenschaftlicher Praxis“ bzw. in der Satzung der Universität Stuttgart zur „Sicherung der Integrität wissenschaftlicher Praxis und zum Umgang mit Fehlverhalten in der Wissenschaft“

Acknowledgments

Thanks to Simon, Tuba, Guillaume, Jan, Tobi, Rafa, Marina, Lothar and all the rest of my DLR work friends and colleagues, who really make the team feel like a family. Also to my other friends in Almeria, specially Bea and Xavi, who have made my time there been one of the most wonderful periods of my life. If I had to choose my own groundhog day, It would be for sure one of those I have spent with you guys.

Kurzfassung

Diese Masterarbeit beschreibt die Prozesse zur Analyse und Charakterisierung optischer Leistungs- und Degradationsmuster verschiedener Beschichtungen, die als Sonnenstrahlungsabsorber für verschiedene CSP - Technologien eingesetzt werden sollen, um Wege zu finden, ihre Leistung und Haltbarkeit zu verbessern und die Verbreitung von dieser erneuerbare Energie durch die Senkung ihrer Kosten.

Im Arbeitspaket 3.1 des RAISELIFE-Projekts wurden mehrere experimentelle Absorberbeschichtungen (basierend auf T91- und VM12-Edelstahlsubstraten) auf einem Parabolspiegelprüfstand getestet, um deren Abbauverhalten und optische Leistungen bei konzentriertem Sonnenlicht zu bewerten. In diesem Dokument wird beschrieben, wie der gesamte Prozess in Bezug auf das Design, den Aufbau und die Ausführung von Experimenten durchgeführt wurde. Es enthält eine detaillierte Beschreibung der Prüfstand-Instrumentierungssoftware, einschließlich der frühen Problemerkennung und weiteren Redesigns und Modifikationen. Es enthält auch detaillierte Verfahren zur experimentellen Tiefencharakterisierung des konzentrierten Solarflusses der Testbench und deren Vergleich mit ihren Vorhersagemodellen. Es untersucht die Möglichkeit der Radiometerintegration zum Schließen des Flussregelkreises unter Verwendung dieser Charakterisierungen und listet zuletzt Laborkampagnen und Analyseergebnisse auf.

Abstract

This master thesis describes the followed processes to analyze and characterize optical performance and degradation patterns of different coatings intended to be used as solar radiation absorbers for different CSP technologies in search for improvevents in their performance and durability and enabling the widespread of this renewable energy by reducing its cost.

Within RAISELIFE project's work package 3.1, several experimental absorber coatings (based on T91 and VM12 stainless steel substrates) were tested on a parabolic dish test bench in order to evaluate their degradation patterns and optical performances under concentrated sunlight. This document describes how the complete process was carried out concerning experiment design, setup and execution. It includes detailed description regarding the test bench instrumentation and control software, including early problems detection and further redesigns and modifications. It contains as well detailed procedures followed to experimentally in depth characterization of testbench's concentrated solar flux and its comparison with their prediction models. It explores the possibility of radiometer integration for closing the flux control loop using those characterizations and, as last, it details laboratory campaigns and analysis results.

Contents

Kurzfassung	I
Abstract	II
Nomenclature.....	IV
1.1 Abkürzungen / Abbreviations.....	IV
Indices/Symbols	V
2 Introduction	1
2.1 Concentrated Solar Power Technology.....	1
3 Theoretical Essay.....	7
3.1 Physics of Solar Absorbers.....	7
3.2 Sample Thermal Cycling on a Solar Concentration Testbench.....	10
3.3 Measuring Concentrated Solar Fluxes.....	11
3.4 CCD Method.....	12
3.5 Laboratory characterization	15
4 Experimental Essay	17
4.1 Chronology.....	17
4.2 Hardware	19
4.2.1 Sample probes.....	19
4.2.2 Test bench configuration	20
4.2.3 Test bench operation	22
4.3 Sensor assembly	24
4.4 Data analysis software.....	27
4.5 Experimental Flux Measurement: CCD Method.....	34
4.6 Experimental Flux Measurement: Flux Map calibration	39
4.7 Experimental Results: First Campaign	44
4.8 Experimental Results: Second Campaign	45
5 Conclusion and Outlook.....	48
Bibliography.....	49

Nomenclature

1.1 Abkürzungen / Abbreviations

Abbreviation	Meaning
CCD	Charge Coupled Device
CPV	Concentrated Photovoltaic Solar Power
CSP	Concentrated Solar Power
DLR	Deutsches Zentrum für Luft-und-Raumfahrt (German Aerospace Center)
DNI	Direct Normal Irradiance
IR	Infrared
LCOC	Levelized Cost of Coating
LCOE	Levelized Cost of Energy
NIR	Near-Infrared
PV	Photovoltaic Solar Power
T91	Metal alloy [X10CrMoVNb9-1]
UV	Ultraviolet
VIS	Visual
VM12	Metal alloy [X12CrCoWMoVNb12-2-2]

Indices/Symbols

Symbol	Description	Units/Value
Q_{sol}	Available solar flux	W/m ²
α_{sol}	Solar weighted absorptance	Dimensionless, 0...1
$\eta_{coating}$	Net efficiency of the absorber coating	Dimensionless, 0...1
ε_{th}	Thermal emittance	Dimensionless, 0...1
σ	Stefan Boltzmann constant	5.67*1e-8 W/m ² .K ⁴
T_{abs}	Absorber temperature	K
λ	wavelength	nm
$\alpha(\lambda)$	Spectral absorptance	Dimensionless, 0...1
$G_{sol}(\lambda)$	Spectral solar irradiance, according to ASTM G173-3, direct irradiance at an air mass of 1.5	W/m ² .nm

2 Introduction

2.1 Concentrated Solar Power Technology

Concentrated solar power (CSP) technology is a kind of renewable energy that exploits the sun's energy by transforming it into thermal or electrical energy usable by our society. CSP bases its working principle in rising the temperature of a certain working fluid, for instance molten salts. This fluid is pumped through a receiver, on which solar radiation is concentrated by mirrors. The fluid thermal energy is transformed to electrical energy, using one of the conventional thermodynamic power cycles, for instance Rankine or Stirling

CSP has some advantages over photovoltaic technology, mainly based on its high cost-efficient capability of storing energy as temperature within the working fluid, which minimizes or even cancels one of the biggest issues of photovoltaic technology: the difficulty of storing energy excesses during production peaks and therefore the incapacity to homogenize energy production along the radiation cycles, such as daily and seasonal variations. This forces photovoltaic power to ultimately depend on more versatile power sources, such as natural gas, which are usually not renewable [1].

CSP can face this problem by storing large amounts of heated fluid (order of MWth) and use this stored heat during night or cloudy periods to still be able to feed the power cycles for producing electricity, making the CSP probably the only self-sufficient renewable energy production technology nowadays, beside Hydropower, which is also a renewable energy source with integrated storage, considered in most statistics as "traditional renewable", with an estimated cost below 0.05\$/kWh [2]. However, potential for new sites is obviously limited for Hydropower, while CSP could be installed on many continents where desert areas are available.

Instead of being converted into electricity, the thermal energy can also be used straight away for any other industrial process that requires it, such as water desalination, drying, cooling or steam processing [3]. Since the most important factor is the required temperature difference or "temperature lift", CSP is optimal for medium-high temperature processes, above 100 °C in sunny regions.

To achieve power concentrations that enable those processes, many families of solar reflector concepts exist. The main ones are:

- Parabolic through:



Image 1. Parabolic through. Andasol 3. Southern Spain. [4]

It is basically a mirrored parabolic surface that concentrates sunlight along a linear absorber tube through which a fluid flows. The working fluid heats up while moving across the tube and is pumped to the storage or power block unit. Several of these concentrators are usually set up in parallel-series blocks in order to maximize fluid output temperature. Most commercial CSP plants use this technology nowadays [5].



Image 2. Set of parabolic through arrays in Andasol 2 [6]

- Solar Towers:



Image 3. Gemasolar plant. Seville, Spain [7]

In this case, a wide field of 2-axis tracking mirrors (heliostats) concentrate their beams onto a central receiver usually located on top of a tower through which the working fluid flows.

Research on Power Towers is yet been carried on. Their efficiency and maximum achievable temperatures are superior, but the radiation density usually means extreme working conditions at the receiver, meaning also a challenge in their design and maintenance. Heliostat deployment isn't either trivial. Due to shadowing, blocking and atmospheric attenuation effects, reflected radiation can drop significantly for the most outer heliostats. Distance between heliostats must increase as they are set up further away from the receiver tower, meaning that the practical value of ground usage drops down below 50% in most of such power plants [8].

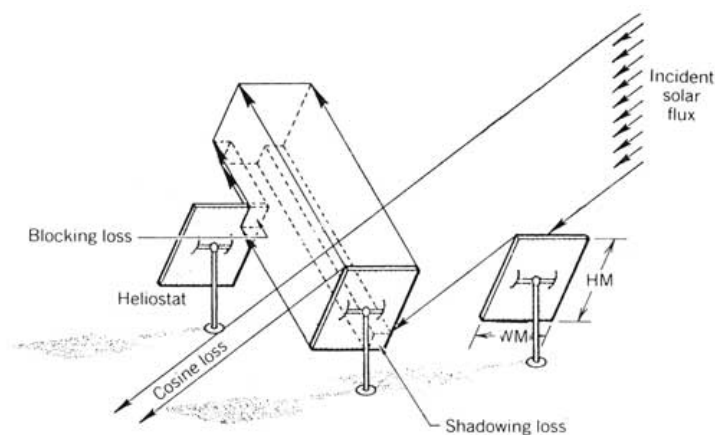


Figure 1: Different flux losses in an heliostat field. [9]

Maximum achievable temperatures and efficiencies have been well studied by the industry. The following figure [8] illustrates the maximum theoretical rates for different concentrator technologies:

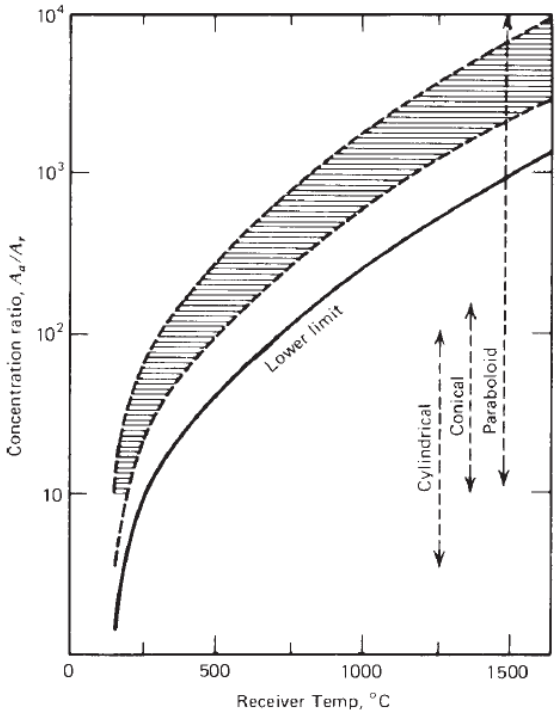


Figure 2: Suitable receiver operating temperatures for different concentration ratios. This figure is orientative and it is shown to illustrate a comparison of different concentrator types [8].

By comparison to its natural competitor, PV technology makes use of diffuse radiation, expanding the potential markets since a lot of countries have reasonable global solar irradiance levels but only a few have reasonable high DNI levels above 1800 kWh/m².year. For the same reason, tracking systems on PV facilities are not always required to reach reasonable effectiveness levels whereas for CSP they're absolutely essential. In addition, CSP deployment is much more technically challenging. Its overall effectiveness is much more sensitive to operation modes and degradation processes and therefore, it's only feasible in an industrial way, being this a great counterpart when comparing it to photovoltaics, which can be usually integrated into small scale networks very easily.

Dealing with those technical challenges makes CSP technology yet hard to compete in production costs with other technologies within the current power market. In this sense, current researches are focused on improving the performance and durability of these systems via efficiency improvement and cost reductions. Current record price was achieved in 2017 for a project call in Middle East, being 0.73 \$/kWh LCOE with 15 hours of storage [10].

Levelized Cost of Energy (Abbreviation: LCOE) [2] is the indicator used to consistently compare different methods of energy production. It is the ratio of the facility's overall lifetime building and operation costs over the total electric energy produced on that period of time.

Following figures shows LCOE comparison of different current technologies, as of 2013:

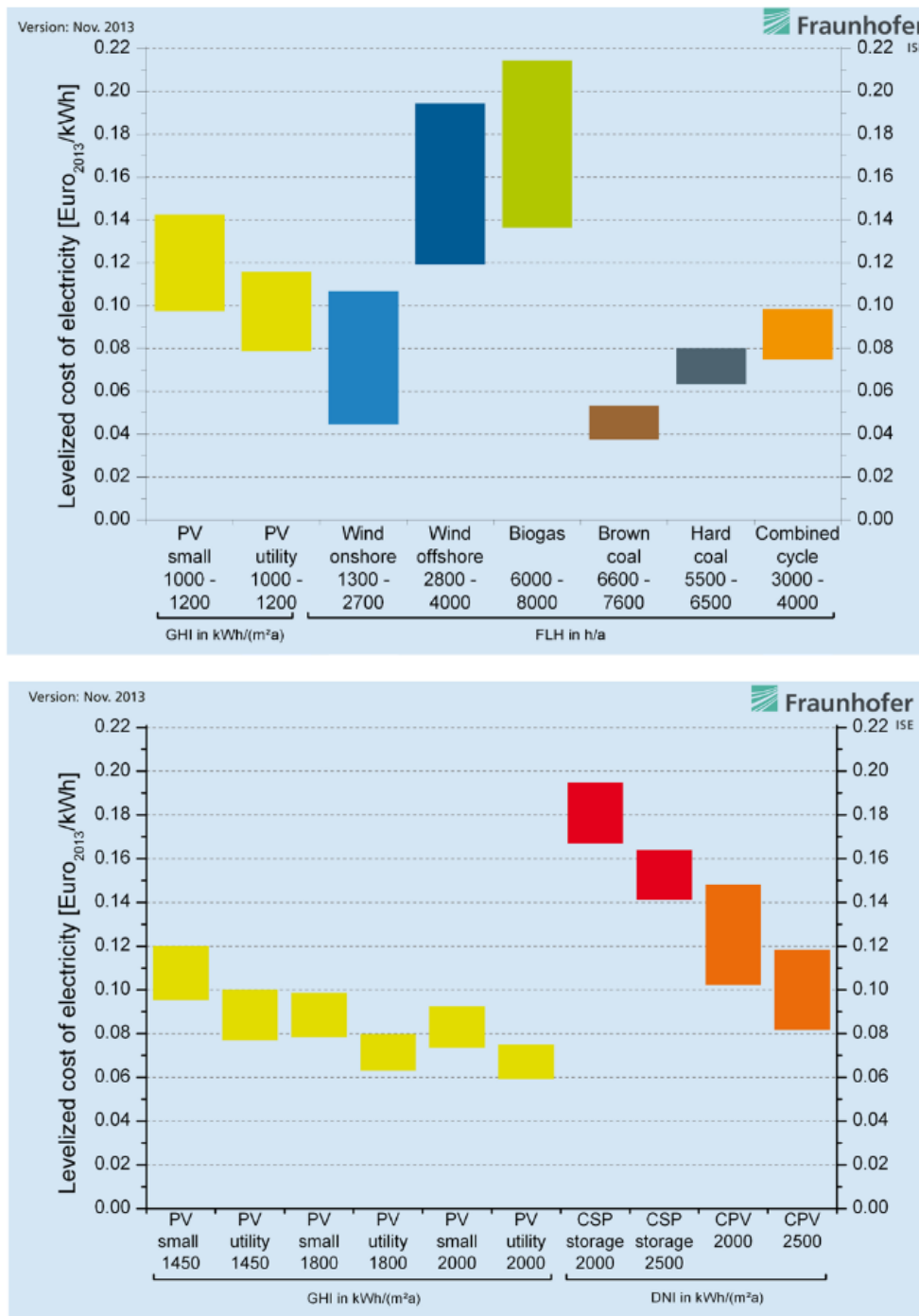


Figure 3: Costs of electricity production for different renewable technologies. Source [8]

From those figures it can be noticed that the key barrier for CSP to be definitely introduced into industrial power generation networks is the LCOE. As shown, CSP+storage technology can be up to twice more expensive than photovoltaics in terms of price/kWh under the same environmental and weather conditions and between 2 and 4 times more expensive than coal based production.

The Levelized Cost of Coating [11] (LCOC) is a new parameter first introduced in 2015 with the aim of comparing the economic performance of different absorber coating technologies. It is defined as the annual cost of a certain coating over the average annual thermal energy produced by the receiver. According to this study, the baseline LCOC using Pyromark 2500 [12], which is the standard coating used in the industry until now, was found to be \$0.055/MWh_{th}, and marginal costs were determined in a probabilistic analysis to range from -\$0.09/MWh_{th} to \$1.01/MWh_{th} [11]

This study also identifies a ranking of factors influencing the LCOC:

- *Initial Solar absorptance;*
- *Thermal emittance;*
- *Degradation rates*
- *Re-application interval, reapplication cost and downtime during re-application.*

Since the introduction of LCOC, scientific effort has focused into developing materials which minimize this parameter. DLR collaborates with other project partners in the development of new experimental coatings following this direction. In our case, 4 different organizations have provided tubular coated sample probes.

Our primary goal is to test those samples under accelerated cycles and evaluate their performances regarding the main factors affecting LCOC: solar absorptance and thermal emittance as well as their degradation patterns. Detailed LCOC estimation requires also deep evaluation concerning economical aspects derived from manufacturing and maintenance costs as well as production losses during maintenance operations. These estimations are however inapplicable since our experimental samples are prototypes and there is no industrial available data regarding those aspects.

The aim is to guide future research lines towards coating technologies which show significant improvements in initial solar absorptance, thermal emittance or degradation rates during these experimental tests.

Detailed information about the prototype samples is confidential and therefore many data regarding their technology and performance is only partially disclosed in this document. Information about the carried out tests, employed techniques and devices, as well as laboratory tests and results are part of DLR knowledge and will be described in detail here.

This document describes two test campaigns performed on two separate absorber sample sets. It shows and explains the processes, techniques, facilities and instruments employed during this process and discusses the obtained results, conclusions, and the further steps to be taken in future research lines.

3 Theoretical Essay

3.1 Physics of Solar Absorbers

As described in previous chapter, main factors affecting absorber's efficiency are initial solar absorptance, thermal emittance and degradation rates.

The Initial solar absorptance is the proportion of incoming radiation absorbed by the absorber and transformed into thermal energy straight away. It is called initial because its value decays over time due to material degradation under working conditions.

Thermal emittance is the amount of energy released due to the absorber's own temperature. Following lines describe how both are related to the absorber's overall efficiency as well as the strategies to be used to maximize it.

According to Kirchhoff's law of radiation:

$$\epsilon_{\lambda} = \alpha_{\lambda} \quad \text{Eq. 1}$$

Which means that given a particular wavelength (λ), good radiation absorbers on that wavelength will be good emitters as well on that same wavelength. This is therefore discourgeous in terms of finding or developing a good radiation absorber, since it will radiate back part of the gathered power as it heats up. There still exist some called selective coatings [13] which are very good absorbers at shorter wavelengths and very bad at longer ones:

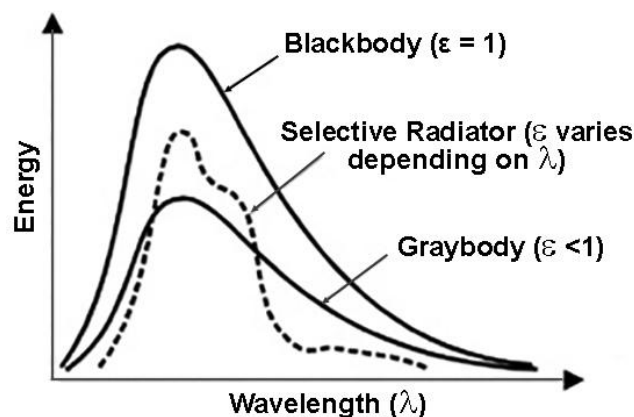


Figure 4: Comparison of selective bodies Planck curves with those of typical Black and Gray bodies [14]

Having low emittance at longer λ (IR) diffcults energy release at lower temperatures, and allows the material to store more thermal energy increasing its overall thermal efficiency by some percentage points as it will be shown in the following pages.

The main idea behind CSP is to transform radiation into heat (absorption), and then transfer this heat to the working fluid as fast and efficiently as possible (conduction). The coating is responsible of the absorption process, and the substrate over which it is spread conducts the collected thermal energy to the working fluid.

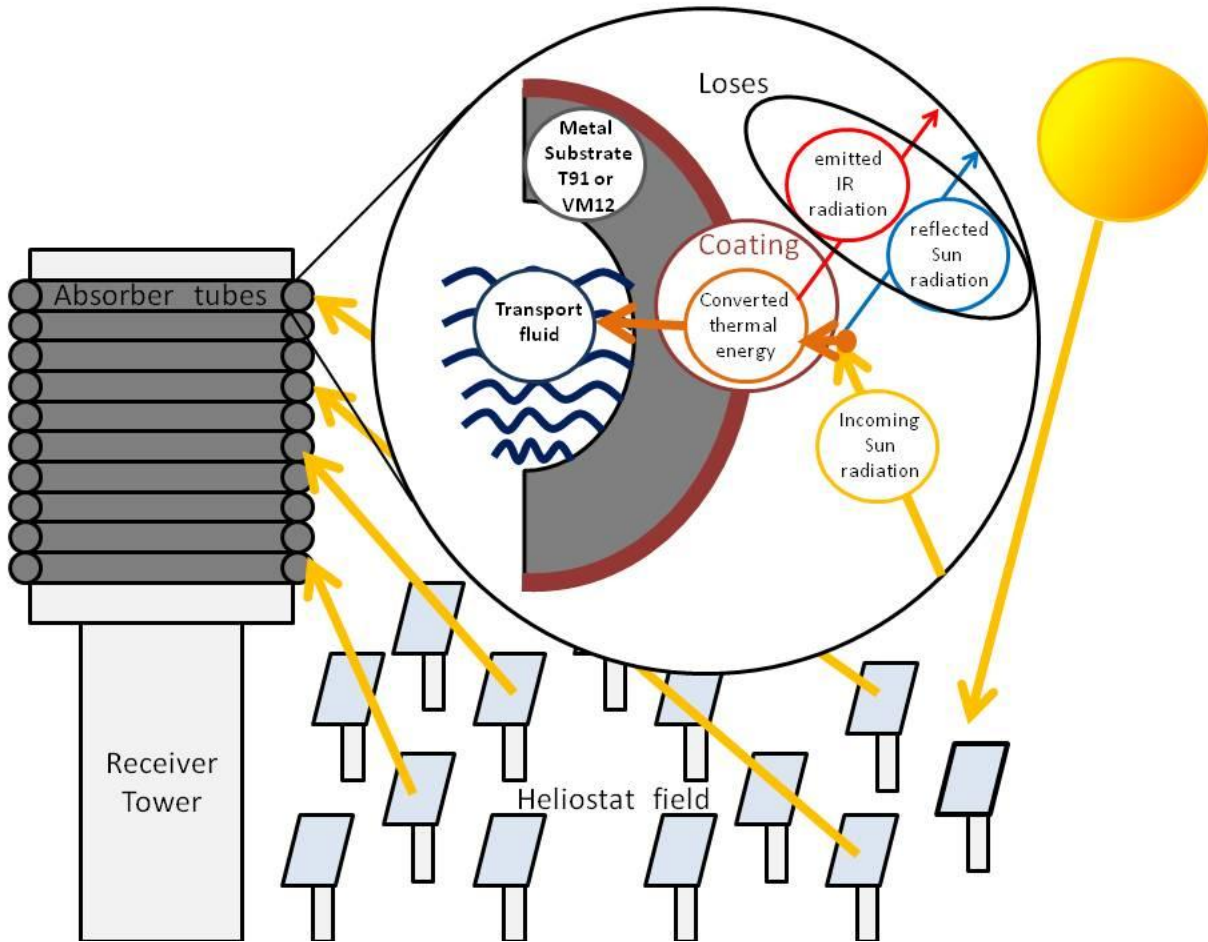


Figure 5: Energy transformation processes, from radiation to fluid heat.

Matter which is irradiated by electromagnetic radiation interacts with it absorbing a portion of its energy and reflecting another portion (Depending on these proportions they are characterized whether as absorbers or reflectors). The portion of power which is absorbed is:

$$Q_A = \alpha_{sol} \cdot Q_{sol} \quad \text{Eq. 2}$$

Which is then stored in the body as thermal energy, rising its temperature. This stored thermal energy is collected by a heat transfer fluid. However, an additional part of this absorbed thermal energy is emitted back according to Planck's Law of Radiation, so the actual net absorbed power would be:

$$Q_{net} = \alpha_{sol} \cdot Q_{sol} - \epsilon_{th} \cdot \sigma \cdot T_{abs}^4 \quad \text{Eq. 3}$$

The absorber's **thermal efficiency** is defined as the net absorption over the total incident concentrated solar flux:

$$\eta_{coating} = \frac{\alpha_{sol} \cdot Q_{sol} - \epsilon_{th} \cdot \sigma \cdot T_{abs}^4}{Q_{sol}} \quad \text{Eq. 4}$$

If we perform a sensibility analysis on Eq. 4:

$$\frac{\partial \eta_{coating}}{\partial \alpha_{sol}} = 1; \quad \text{Eq.5}$$

$$\frac{\partial \eta_{coating}}{\partial \epsilon_{th}} = -\frac{\sigma T_{abs}^4}{Q_{sol}} \quad \text{Eq.6}$$

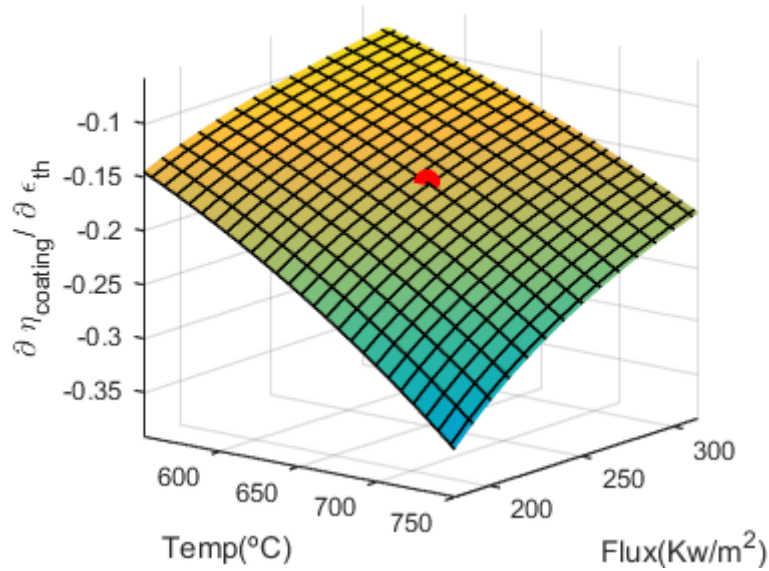


Figure 6: dependance of $d\eta/d\epsilon_{th}$ relative to temperature and flux values.

Assuming operation conditions of 650°C surface temperature (typical in solar towers) and 250 kW/m² solar flux, $d\eta/d\epsilon_{th}$ would be -0.165. **This means that 1% improvement in absorber's overall efficiency can be achieved by whether enhancing its solar absorptance by 1% or by decreasing its thermal emittance by 6% (that is 1/0.165).**

3.2 Sample Thermal Cycling on a Solar Concentration Testbench

During the tests, experimental samples are supposed to be exposed to a set of conditions which are representative from those expected during their expected lifespan. These conditions are defined by consensus with other project partners and their ultimate reasonings are not to be discussed in this work.

Sample probes shall be mounted on a test bench capable to provide them with an adjustable level of concentrated solar flux (at least 250 suns at peak point) and a temperature control system (air cooling system).

By using those two degrees of freedom, the test bench must be able to perform exposure cycles following specified flux and temperature setpoints. Following figure shows defined setpoints during first and second test campaigns:

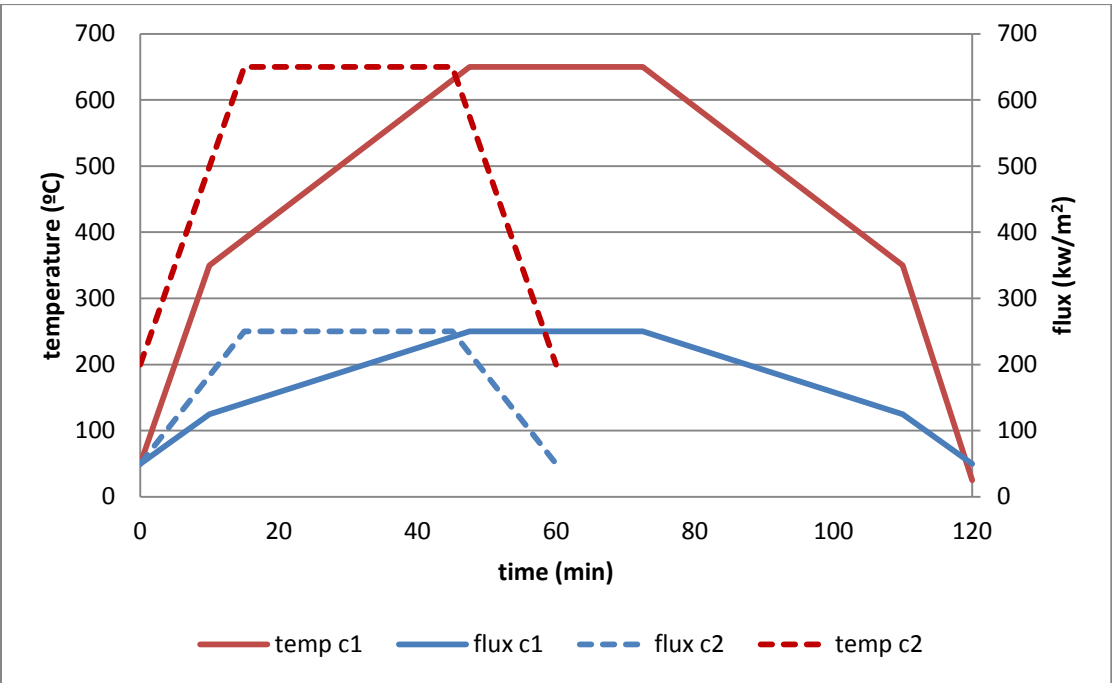


Figure 7: Flux and temperature setpoint curves across one exposure cycle.

Number of cycles per campaign was set to be 100. Every 10 cycles, samples must be carried from the test bench to the laboratory to perform a series of analysis to measure solar absorptance and thermal emittance and photographing coating surface at the microscope.

The ultimate goal is to measure the decay of those variables over time to rank the coating’s performance according to thermal efficiency and LCOC definition.

Real implementation of this test bench model as well as its performance description is covered in chapters 4.2.2 and 4.2.3

3.3 Measuring Concentrated Solar Fluxes

Usually, mirrors used in CSP technology are far from being perfect since high mathematical perfection in their reflective patterns is not required for CSP systems to still achieve really high efficiencies in terms of energy conversion. These imperfections however imply high flux inhomogeneities in the volumetric area surrounding the focal point and therefore difficulties in terms of predicting spatial flux distributions. Following figure shows an ideal flux pattern (when defocused) generated by a perfectly shaped parabolic mirror, compared with the observed pattern of the paraboloid dish mirror.

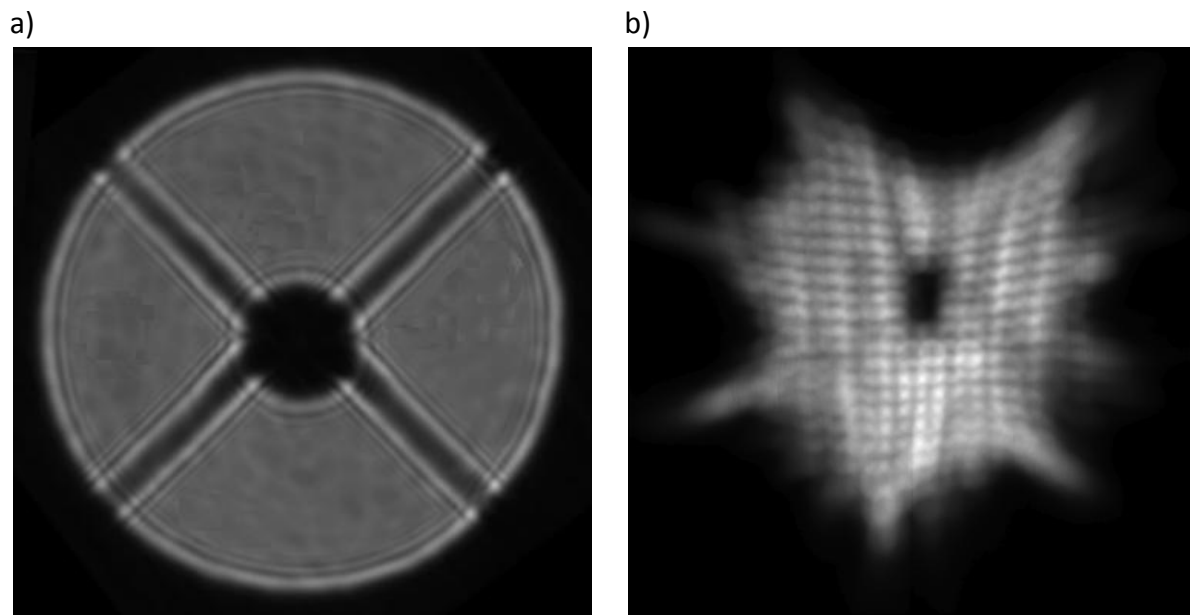


Figure 8. a) Flux pattern generated by a defocused ideal parabolic mirror (defocused telescope's grade primary mirror). The center dark area is the shadow produced by the secondary mirror. b) Flux pattern generated by defocused paraboloid dish mirror. Center dark area is the shadow produced by the test bench.

Flux distribution can be observed by moving the test bench back and forth along the focal axis using a linear drive.

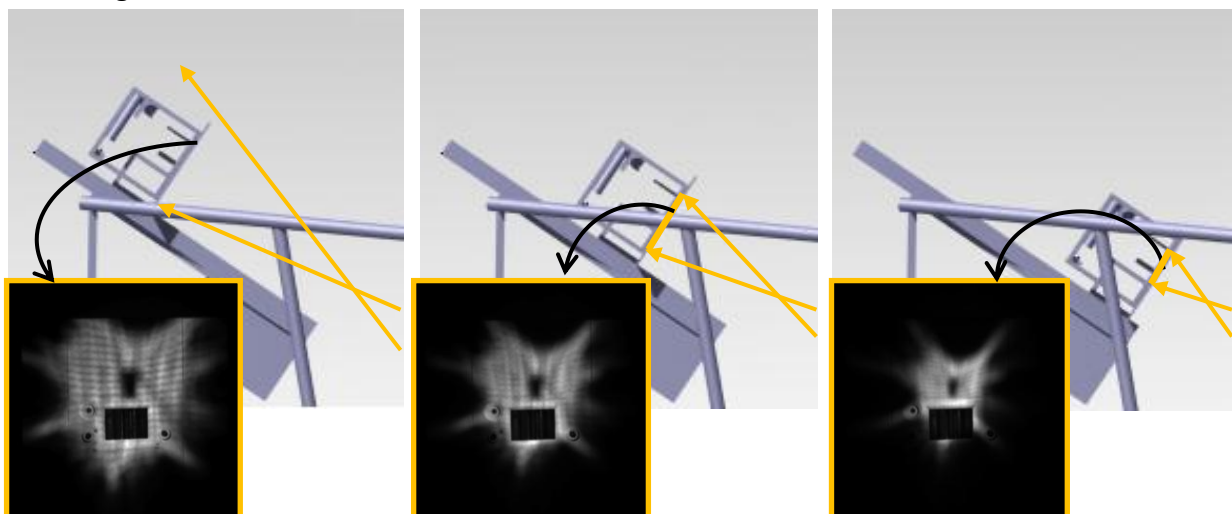


Figure 9: Flux patterns at different focal positions (real experimental data).

Since these flux asymmetries would obviously imply different experimental conditions for each sample, some possibilities for homogenizing the flux were considered. One of them was to add a kaleidoscope at the focal point. There has been previous kaleidoscope experiences aiming to homogenize flux inlets, and the results were quite satisfactory although not perfect. However, due to the high power concentration rates of the Distal II dish, any kaleidoscope should be actively refrigerated, otherwise it would not hold the high temperatures induced by the absorbed flux. Other solutions would consist on using some kind of mobile or rotating sample tray, somehow moving across the flux maps, to blur the effects of its inhomogeneities.

These ideas however would have implied major hardware modifications and re-design, and we kept thinking in search of a more economic solution in terms of manpower and effort. It was thought that if flux homogeneity could not be assured, **it should be found at least a way to accurately track the flux being applied on each sample**. By doing so, we could in first place relate sample's degradation to their received flux dosis, and, additionally, we could include real flux feedback into the test bench flux control loop.

3.4 CCD Method

This section describes some particular techniques used to measure and characterize concentrated solar flux. Those are described in details in a PhD thesis work [15]. Additional information, including achievable accuracy studies and error budgets can be found in the aforementioned document.

We've seen that knowing the 3D distribution of the reflected solar flux would allow us to keep track of how much radiation each sample collects during a certain cycle. This however, has always been a major problem in the CSP industry. Measuring the solar flux with enough spatial and power resolution is a problem that many experts have been dealing with over the last few years. Due to the depth of this topic, many concepts and reasonings will not be disclosed in this document, but they will be referenced to previous works [16].

Known flux measurement methodologies can be essentially divided into two categories: direct and indirect methods. Direct methods can be based on many different strategies (calorimetry, thermocouples, photoelectric effect) but they all employ sensors that read actual flux values at the position where they are located. Indirect methods, usually based in CCD cameras combined with lambertian reflectors, give very nice readings in terms of power spatial distribution but they cannot provide absolute flux values. In other words, indirect methods have a great spatial resolution, but they can only tell that certain pixels detect twice, three times or just half the power of other certain ones.

Current techniques employ both families of methods. Indirect methods are usually used to get spatial flux distribution maps that are later calibrated using one or many direct methods. Within this project, this was the followed path. First goal was to elaborate a flux

distribution map by using the CCD method, and then calibrate the map with data obtained by a radiometer (direct method).

Before the start of the project there already existed a set of flux distribution map models that were developed previously using raytracing techniques. Their documentation contemplated 25% uncertainty in many cases, ignoring shadowed regions, and because of that, it was decided to go for the CCD method to get flux distribution maps based on experimental data which reduced uncertainty to more reasonable values.

As deeply explained in a PhD thesis [15], the CCD method is an experimental method for measuring spatial distributions of solar radiation fluxes. It consists on measuring the mirror reflection on a lambertian surface using a CCD camera. The flux haze can be intercepted with the lambertian target at different locations and angles to resolve flux's shape in different sections. In this way collections of gray value images are collected, containing a representation of the flux spatial distribution within the intercepted section. When putting all the data together, accurate 3D models can be built.

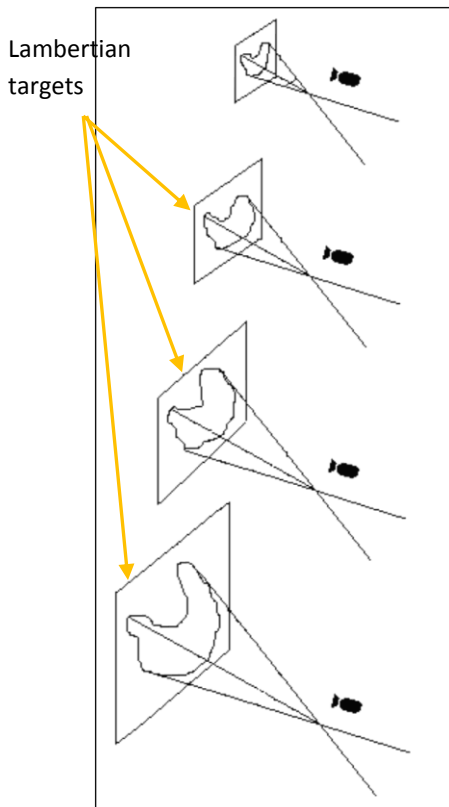


Figure 11 Lambertian reflection patterns at different locations during CCD method application

Step 1: Images of an irradiated lambertian target are taken using a CCD camera

Step 2: The lambertian target is relocated at different positions/angles within the solar haze and new images are taken

Step 3: The collection of gray value images is now correlated to the spatial positions at which the lambertian reflector was located when they were taken.

Step 4: Spatial interpolation between pixel values can now be performed across the control volume to return a reconstruction of the solar flux distribution

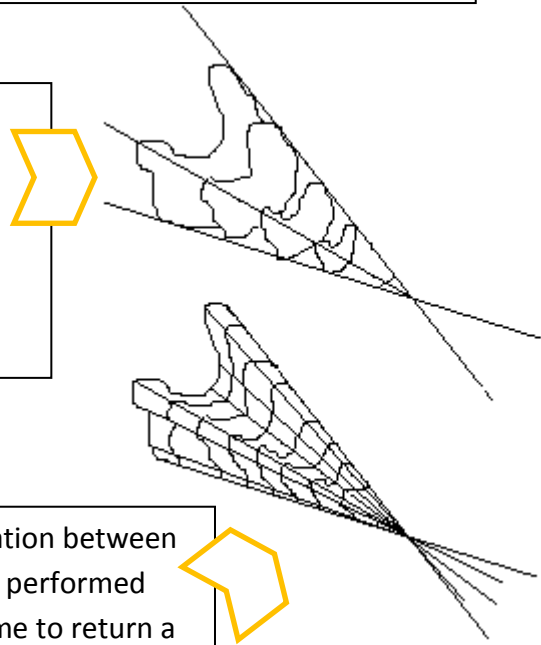


Figure 10 Reconstruction of the spatial flux distribution

There is a way for transforming this set of grayscale images into a set of flux maps (in terms of radiated power) without needing any direct method for the calibration process. Obviously this will result into an estimation, but it will be useful for comparison and double check purposes at the end of the process.

The idea is to distribute the hazes' overall power across the image's gray values. Since we know dish's dimensions and reflectivity, its power shall be always constant and known, and we could now assign a certain power value to each gray pixel value by dividing the overall dish optical power by the overall image gray value sum. Main sources of errors in this method are the errors taken when measuring dish's dimensions and reflectivity, and the uncertainty when determining the absence of spillage (flux being radiated away of the sample tray). These errors can be reasonably high [15] and therefore, data calculated this way **will always be a raw approximation with limited scientific accuracy and reliability. To get more accurate flux maps** (in terms of spatial and power resolution) the existent ones **must be calibrated using experimental data from sensors gathering real readings from at least some locations irradiated by the solar flux.**

Readings of those sensors (radiometers) can be spatially combined with gray value maps to extrapolate approximations of the flux maps with really high spatial and depth resolution.

It is important to notice that errors regarding flux map values on individual pixels can be diluted by up to three orders of magnitude when considering that every sample covers an area in the image of around 1200 pixels (30x40). Even considering a +/-10% flux power error in individual pixels, the overall error on the average power received by a 30x40 pixel sample would be 0.0083%. This sounds far reasonable even considering that no particular error thresholds were specified in the project at this regard.

3.5 Laboratory characterization

Sample optical analysis was performed every 10 cycles in a laboratory during the first test campaign on T91 substrate and every 20 cycles during the second one on VM12 substrates. They consisted of a set of spectral reflectance measurements using spectrophotometers and sets of microscope and large scale images to track sample optical degradation. During the first campaign, only one spectrophotometer was available (Perkin Elmer **Lambda1050** [17], UV+ Visual+NIR 280-2500 nm). For the second campaign, additional data was collected using a second spectrophotometer (Perkin Elmer **Frontier FTIR** [18], IR 2000-16000nm).



Figure 12: Perkin Elmer Lambda 1050 and Perkin Elmer Frontier FT-IR.

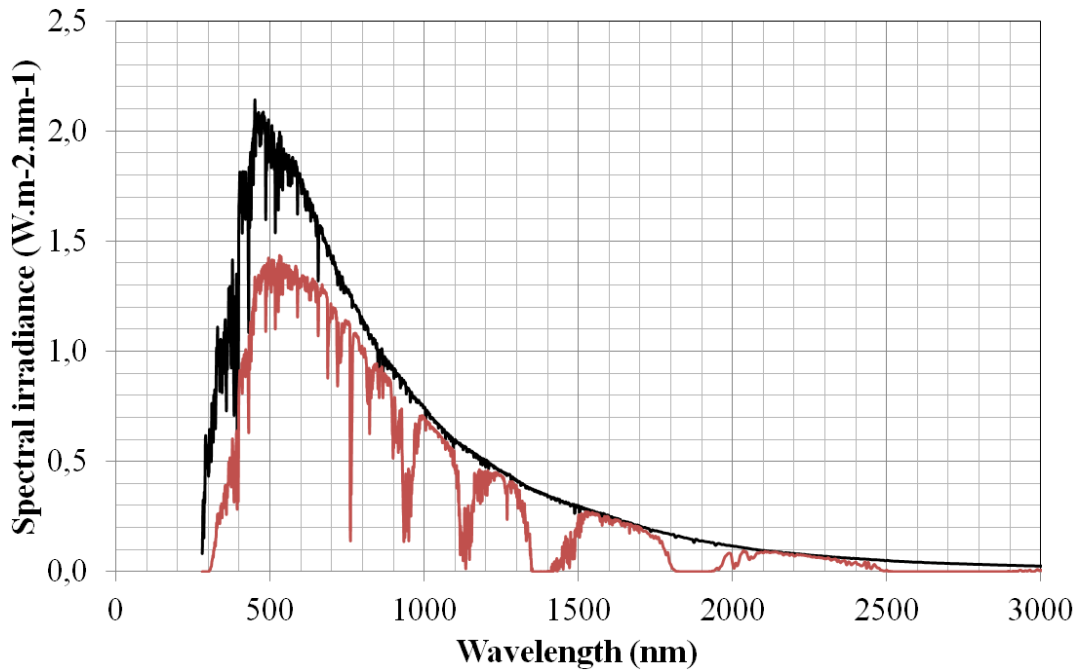
To analyze the sample's absorptance, the spectrophotometer irradiates the sample with a predefined light beam and records the reflected pattern. Since the emitted power is known and the reflected power can be measured, the absorbed power can be accurately deducted for every wavelength and the absorptance as the ratio between absorbed and received power.

According to Kirchoff's law of radiation, absorptance and emittance on a certain wavelength have the same value, so thermal emittance can be calculated following the previous procedure, by just measuring the absorptance over the infrared spectrum.

The **Lambda1050** [17] measures the reflectivity in 5nm band intervals ($d\lambda=5\text{nm}$), and it does it between the limits $\lambda_1=280\text{nm}$ and $\lambda_2=2500\text{nm}$. Absorptance $\alpha(\lambda)$ is then calculated as:

$$\alpha(\lambda) = [1 - R(\lambda)] \quad \text{Eq. 5}$$

where $R(\lambda)$ is the reflectivity value (dimensionless) at particular wavelength λ given by the spectrophotometer. The absorbed power on each λ (Solar absorptance $A_{\text{sol}}(\lambda)$) is the absorptance weighted by the available direct solar irradiance on that λ at an air mass AM 1.5 ($G_{\text{sol}}(\lambda)$), which is shown in the following figure:



— Extraterrestrial Radiation (AM0) — Direct Normal Irradiance (AM 1.5)

Figure 13: Comparison of extraterrestrial (AM0) and direct normal spectral solar irradiance (AM1.5) according to ASTM G173-03 [19]

$$A_{sol}(\lambda) = [1 - R(\lambda)] \cdot G_{sol}(\lambda) \quad \text{Eq. 6}$$

The total solar absorbed power would be therefore the integral of previous expression along the interval λ_1 - λ_2 :

$$A_{sol} = \int_{\lambda_1}^{\lambda_2} [1 - R(\lambda)] \cdot G_{sol}(\lambda) \cdot d\lambda \quad \text{Eq. 7}$$

Finally, solar weighted absorptance ratio α_{sol} would be the total absorbed power over the total available solar power:

$$\alpha_{sol} = \frac{\int_{\lambda_1}^{\lambda_2} [1 - R(\lambda)] \cdot G_{sol}(\lambda) \cdot d\lambda}{\int_{\lambda_1}^{\lambda_2} G_{sol}(\lambda) \cdot d\lambda} \quad \text{Eq. 8}$$

In this way, a unique percentage for each sample is calculated, characterizing the efficiency of each sample when transforming solar radiation into thermal energy.

4 Experimental Essay

4.1 Chronology

At the beginning of the project, an early version of the test bench was available for performing solar cycles. Some flux map models developed in 2011 using ray-tracing simulation and deflectometry measurements were being used to estimate the flux distribution over the sample tray.

- The first task was to develop a software tool for visualizing the flux distribution in a user-friendly way. Data feeding this tool were initially the flux maps obtained by the ray tracing technique.

- First Campaign cycles were performed, experimental data was collected. Test bench data analysis software tool development started.

- First test bench data are evaluated with previous software tool and first flux inhomogeneities and temperature inconsistencies are detected. Some thermocouples show also erratic behaviors.

- Inhomogeneous results motivate the development of an experimental flux map collection. A CCD method is used to take images of a dummy lambertian target under experimental radiation conditions. Some mistakes during technical execution lead to the introduction of higher than desired errors. Still, results are used to elaborate a first experimental flux map version which is integrated into the previous flux maps tool to enable comparison with the first ray-tracing models. Even with the presence of errors, major discrepancies are noticed in both flux maps which lead to think about a systematic underestimation of the ray-tracing model values.

- Faulty thermocouple behaviors motivate trials with different assembly configurations in search of a more reliable mechanical assembly. Temperature reading differences on this newly reassembled thermocouples motivate a further research on the influence of thermocouple assemblies in data readings.

- Temperature offsets are confirmed depending on thermocouple mounting. Most suitable reason for this offset is thought to be the unintended cooling of the thermocouple body by the air flow and their metal clamps inside the refrigeration tubes, as well as a deficient contact (in terms of heat transfer) between the thermocouple's tip and the sample's wall. Longitudinal thermocouple configuration shows higher and much more stable temperature readings, however, it proves our experiments to be exposing the samples to systematic overheating. That was the most suitable reason for the observed coating early degradation.

- Major test is performed comparing clamp-based thermocouple assemblies and longitudinal based ones. Longitudinal ones show up to 200 °C systematic overheat readings. Overheating is confirmed as well in all the previous test rounds. Severe optical degradation observed during the laboratory analysis is definitely attributed to the unintended overheating. It is decided to interrupt the test campaign and report current status to the partners.
- Project Partners decide to abort the current campaign and start a new one, using brand new coated samples based on a different metal substrate (VM12).
- During this interruption, the LabVIEW interface is improved in order to make it more user friendly, safe and robust and thought to be operated by inexperienced users. Its enhanced automation leaves the operator the only decision of starting the sequence or not based on his/her estimation of the weather conditions along the cycle duration; the criteria for starting the sequence are:
 - DNI preferably above 700 W/m² to ensure a sufficient radiation flux
 - Steady-state conditions to perform 1 hour cycles without significant cloud passage
- A radiometer is installed in the test bench and integrated into the interface as well.
- Some Dish mirror facets are slightly shadowed in order to fix flux inhomogeneities, cleaned and its reflectivity is measured using a D&S portable specular reflectometer [20]
- Flux map collection is updated with a new round of tests using an improved version of the CCD method. 12 instead of 8 bit resolution and more systematic and accurate technique are used. On these new flux maps, the mean deviation of the total images' power is now below 3% of the mean value. They now allow to better track the position of individual samples and calibrate flux dosis calculation.
- Laboratory equipment is improved with an infrared spectrometer allowing the characterization of thermal emittance.
- New laboratory measurements show practically inexistent degradation of receiver coatings for the second measurement campaign with VM12 [21] substrate

4.2 Hardware

4.2.1 Sample probes

The samples are special coated metal tubes of 31.8mm external diameter, 40mm length and 5mm thickness. There are 4 coating types provided by different research institutions, each coating type is applied on 3 samples. Due to confidentiality reasons, they will be referred as coatings A, B, C, D from now on. There is one remaining sample type, called reference, which is composed by 3 uncoated tubes, one of which is completely polished. On the first campaign samples were made out of T91 [22] substrates, whereas VM12 [21] were used for the second set.

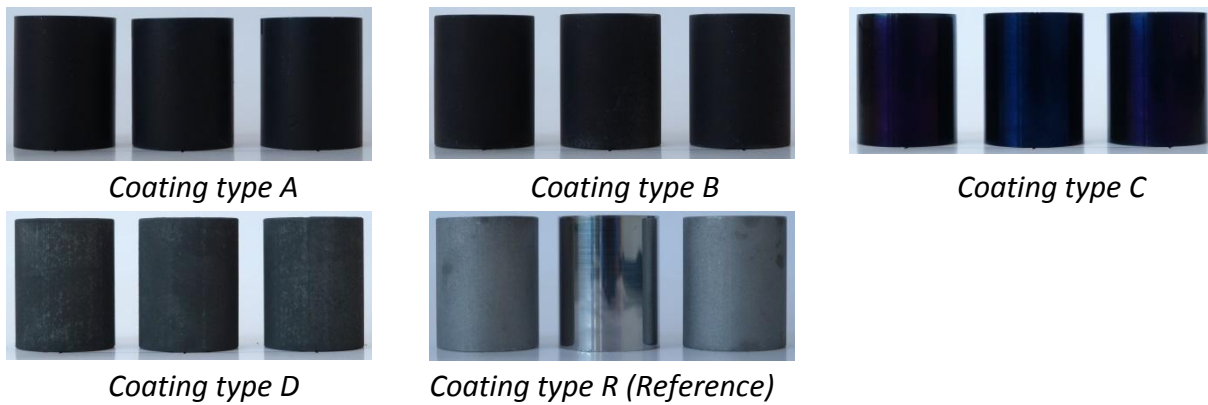


Figure 14: VM12 samples before beginning of the test campaign at the dish test bench.

4.2.2 Test bench configuration

The test bench is a modified parabolic dish solar Stirling system [23]. The original design consisted of a 2-axis tracking 8.5 m diameter parabolic mirror that concentrates sunlight on a focal point at which an Stirling engine was located. The Stirling engine was replaced by an instrumented test bench mounted on a linear actuator.

a)



b)



Figure 15: DISH facility. Left: CATIA model; Right: real picture.

The mirrors are made out of glass and have and have a nominal specular reflectance of 92%, as measured with the D&S portable reflector [20]. Along the symmetry axis and thanks to the linear actuator/drive moves an instrumented test bench holding our samples:



Figure 16: Detail of the instrumented testbench holding the samples.

The test bench moves back and forth from the optical focal point, enabling the adaptation of concentration ratio on the sample set:

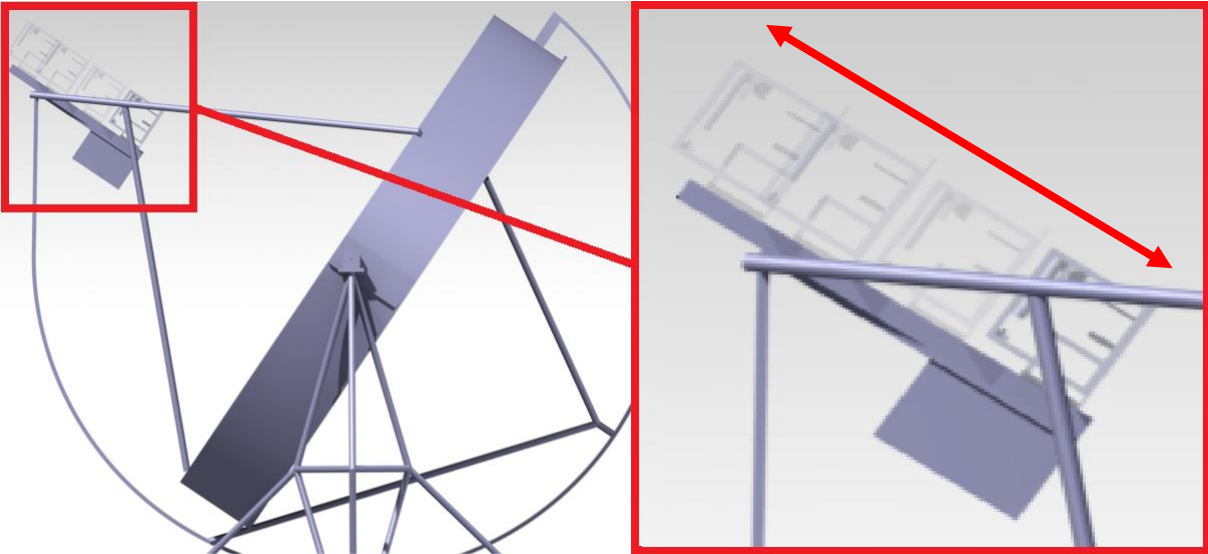


Figure 17: Detail of the focusing/defocusing method.

This test bench consists basically of a metal frame holding the coated samples, the thermocouples, the air cooling system for samples (blowers), and the radiometer and its separate water cooling system. The front part of the frame is covered with a windowed ceramic front protection that prevents anything but the coated samples to be irradiated by the concentrated solar radiation.

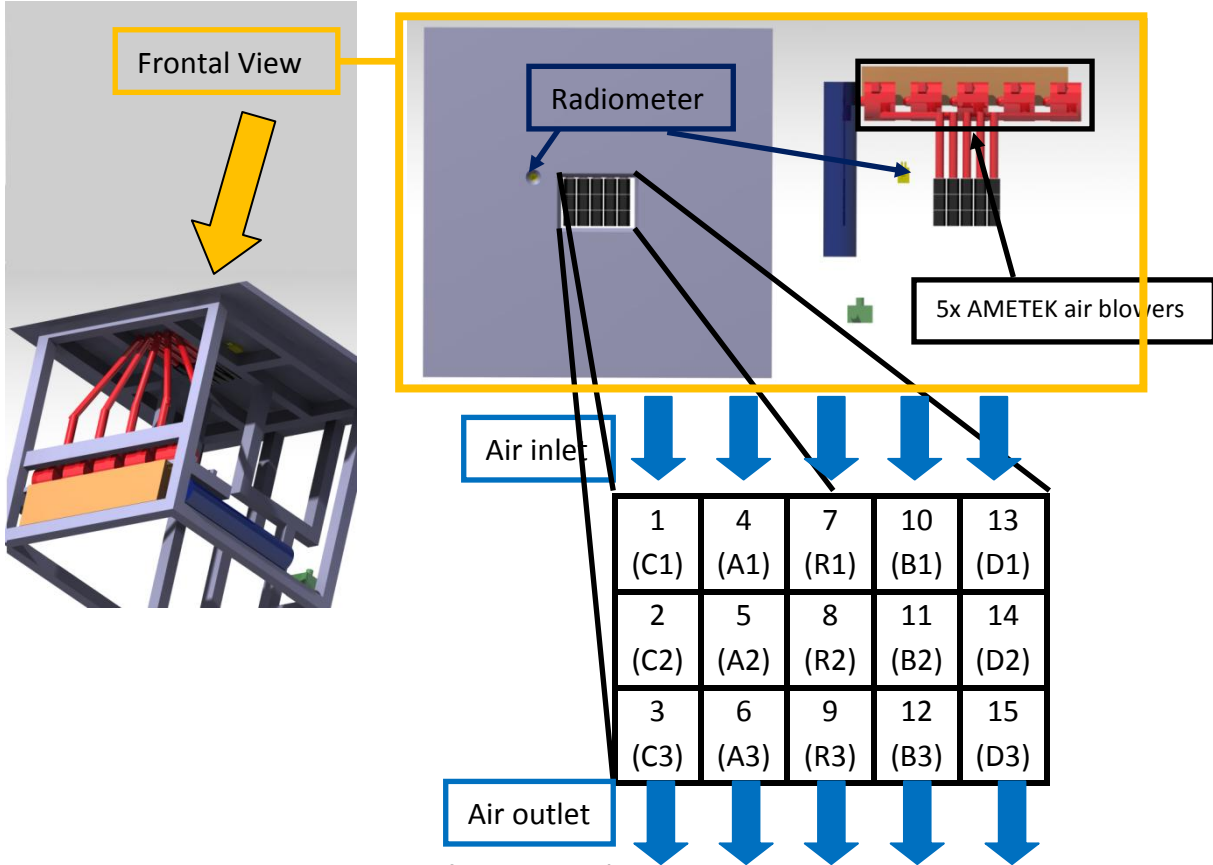


Figure 18: Detail of exact sample's position within the test bench.

On the rear part there is a set of 5 air blowers AMETEK, (with analog rpm control using a 4-10 V control line) responsible of cooling down each of the 5 sample rows and a small CPU water cooling system (1 kW) responsible for radiometer cooling.

The sample temperature is therefore adapted by adjusting the amount of energy that we put into the system (flux adjustment through focal position) and the amount of energy the blowers take away from each of the rows (through blower control voltage).

4.2.3 Test bench operation

The cycling process is controlled by a LabVIEW Interface. The current version was developed from scratch but based on a preliminary one. This new version is more computationally efficient and it allows higher execution rates in control loops and data sampling. It was designed based in user-friendly and high reliability paradigms and enables inexperienced operators to perform tests without risk of accidentally damaging the samples, misusing functions or incurring into unexpected situations.

The program includes functions for handling overheating situations, sensor malfunction scenarios and automatic cycle sequencing. Further improvements on weather forecasting would allow completely self-autonomous experiment execution.

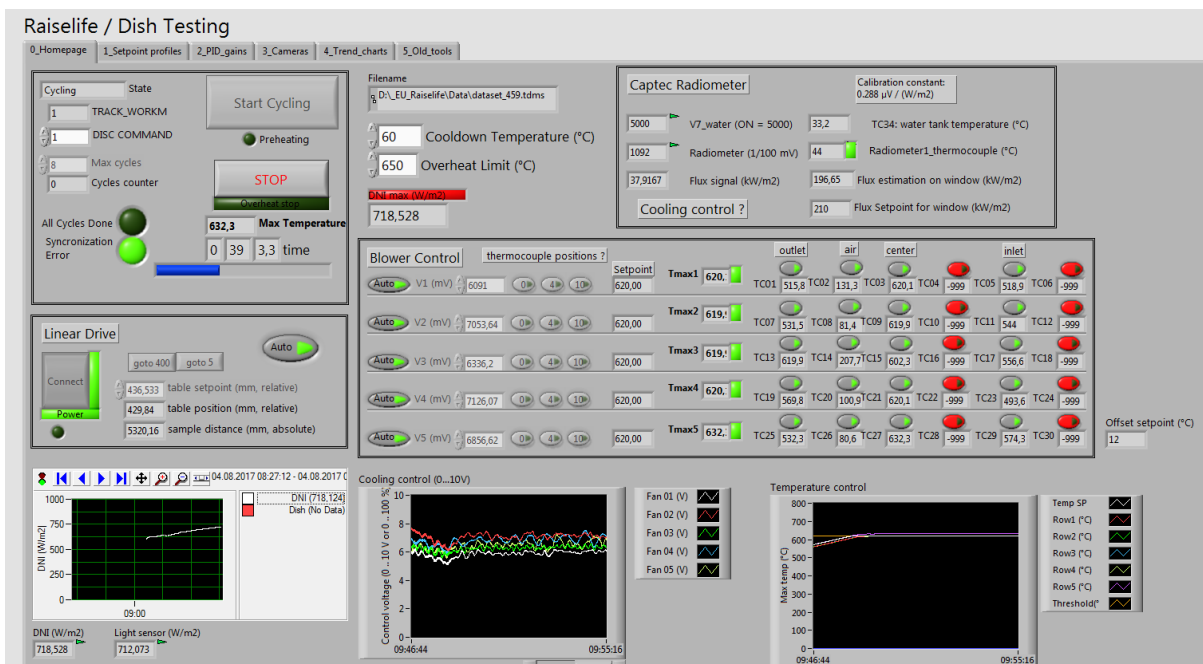


Figure 19: Detail of the control interface's main view.

This LabVIEW interface basically runs two separate control loops, one adjusting the flux, and another one controlling each one of the 5 air blowers:

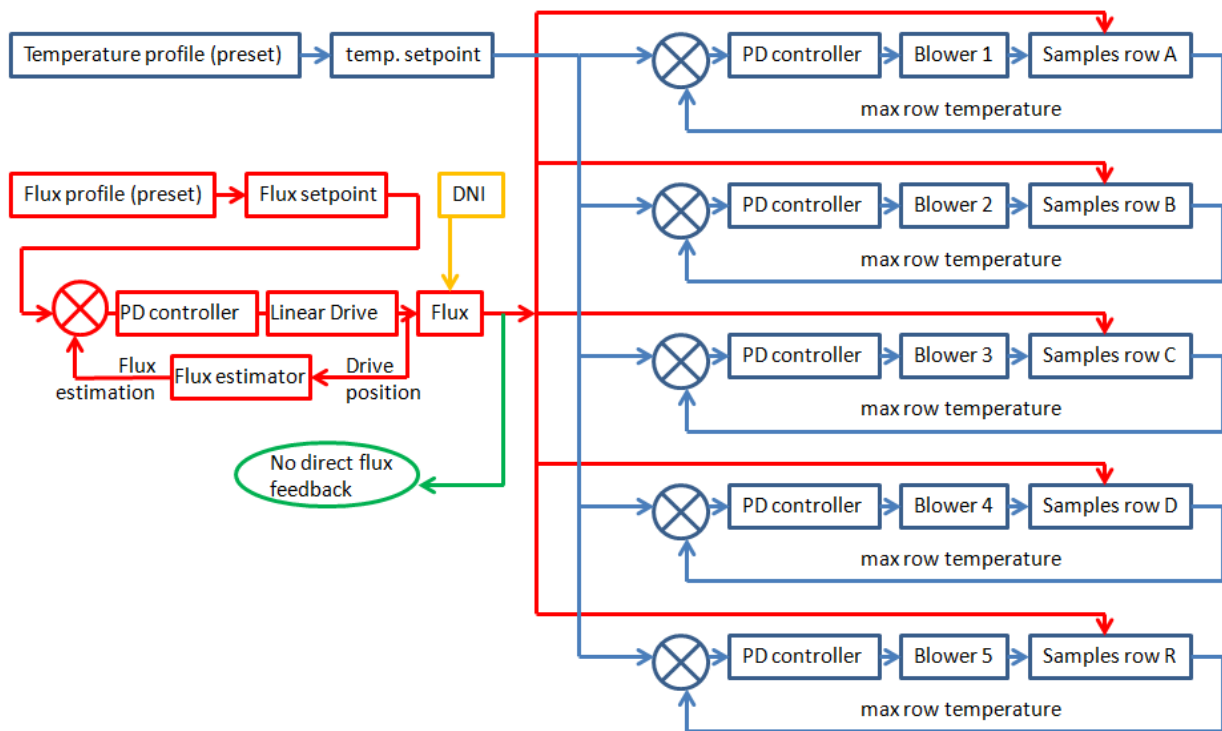


Figure 20: Dish control loop structure.

The Flux control loop pretends to adequate the flux on the window samples according to the established setpoint. In order to do that, since there is no actual flux feedback (there is no sensor) the flux value has to be estimated based on the linear drive position and the available DNI, assuming a constant mirror reflectance. Each one of the secondary control loops actuates on the maximum temperature reading of its row and tries to keep it at temperature setpoint. Those setpoints for the flux power and temperature are not constant, but they follow a predefined evolution in time specified by project specifications (see chapter 3.2).

Second campaign introduced half duration cycles with more aggressive temperature gradients and standby temperature of 200°C.

System operation has proven to be very accurate and reliable in different sunlight and weather conditions as well as to have a good response to transient stages (clouds). **Second test campaign was performed** using this reviewed version of the program **with almost no human intervention** without experiencing unexpected behaviors, sample or test bench damages, bugs or data losses and enabling human workforce relocation to other research activities.

4.3 Sensor assembly

At the very beginning of the first campaign, each sample had two separate thermocouples attached to it. One of them was sensing the temperature of the sample's rear wall and the other was attached to the front wall. The overall setup is illustrated below in Fig. 15:

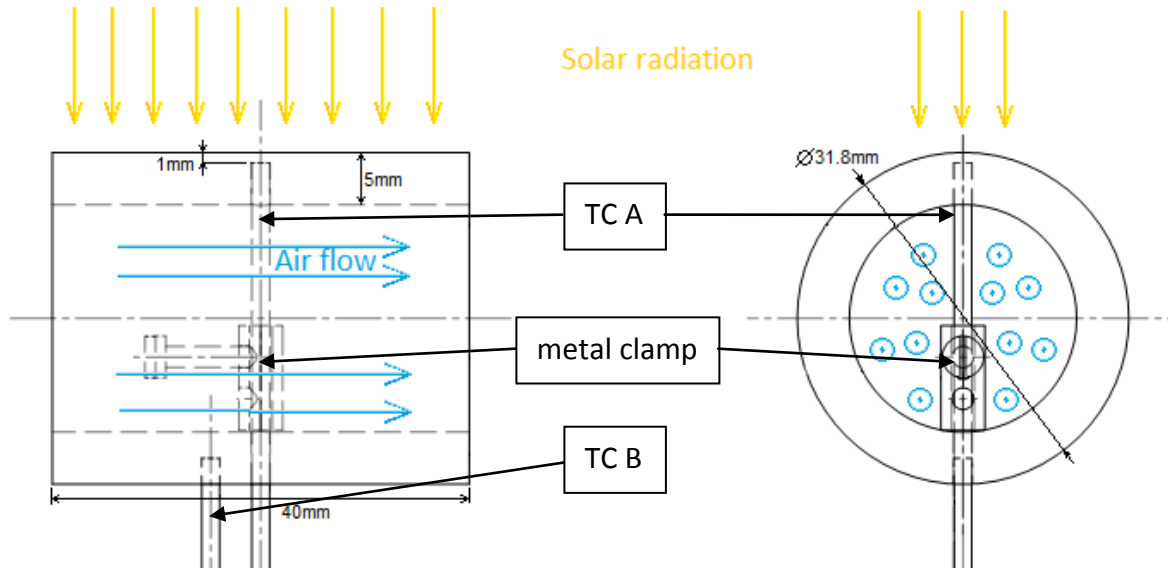


Figure 21: Detail of first thermocouple assembly. A metal clamp is used to hold TCA in place

As shown on Fig. 15, thermocouple A (TC A) was inserted across the rear wall into the front wall at 1 mm distance from the surface and hold there by using a metal clamp. As illustrated on the figure above, part of the thermocouple A body and the clamp were actually into the airflow. This observation was at first not taken into account and its effects on the temperature readings were considered to be negligible. This was lately proved to be a significant error.

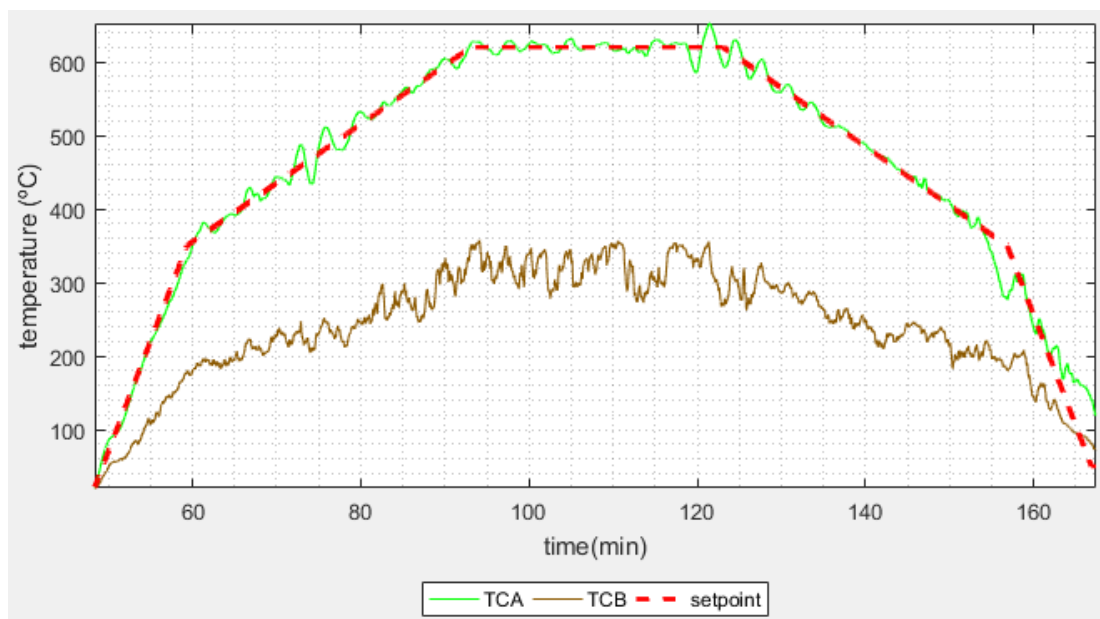


Figure 22: Typical data readings with first thermocouple configuration.

Figure 16 shows typical thermocouple readings during the first 40 cycles on the row consisting of reference samples without coating. Faulty thermocouple behaviors with the previous configuration lead us to assemble one additional thermocouple along the longitudinal direction of the front wall to double check readings reliability:

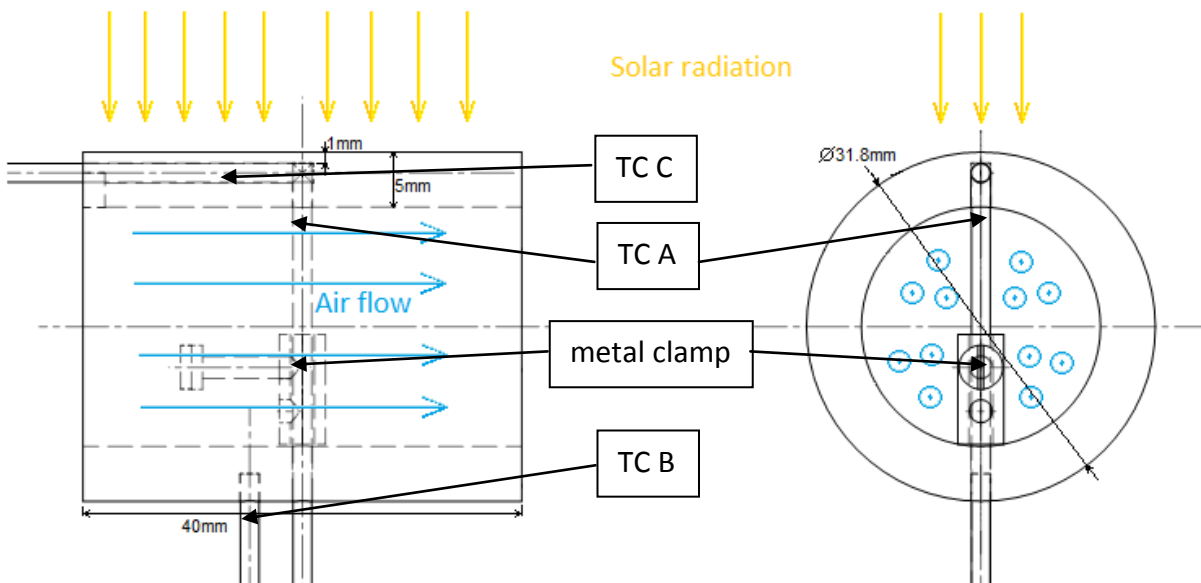


Figure 23: Detail of second configuration. An additional thermocouple TCC is inserted across the front wall.

Starting from cycle 41, two reference uncoated samples were assembled with the previously shown configuration. Their temperature readings during experiment execution where:

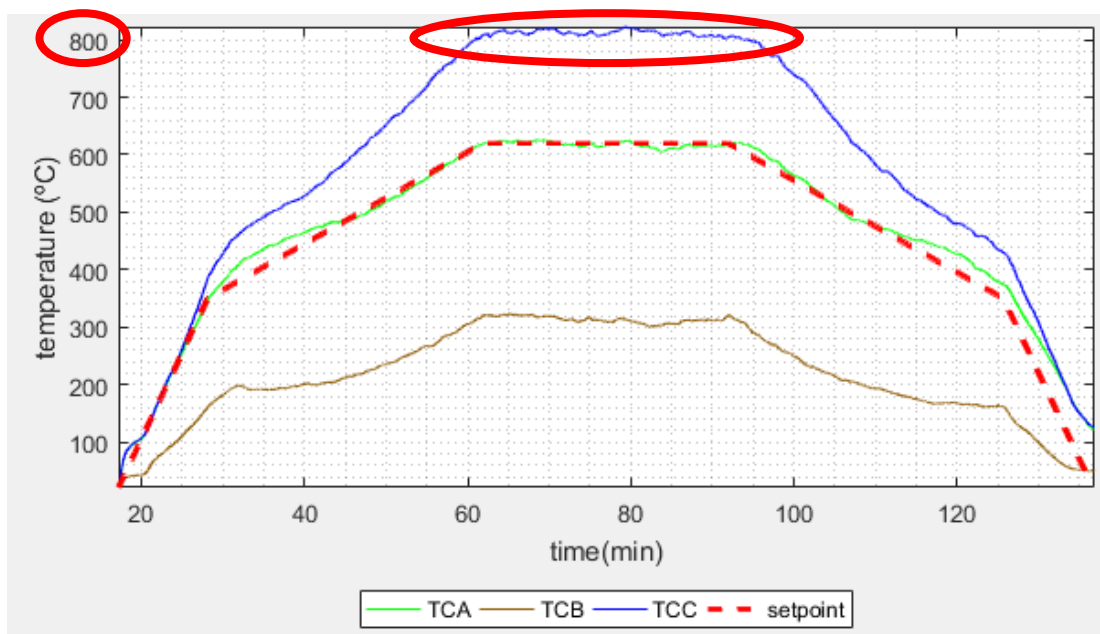


Figure 24: Typical readings with second configuration. The additional thermocouple shows readings 200° over design specifications.

TC A and TC C were supposed to collect similar readings, since they were both attached to the front irradiated wall. But instead of that, the new longitudinal thermocouple read temperatures 200°C higher than the clamped one. This design error had significant consequences, since a strict temperature limit had been set to 650 °C for skin temperature.

If these new readings were right, there had been a 200°C overheating in all the 50 previous cycles. After drilling all samples to introduce the additional TC C, cycle 51 is shown:

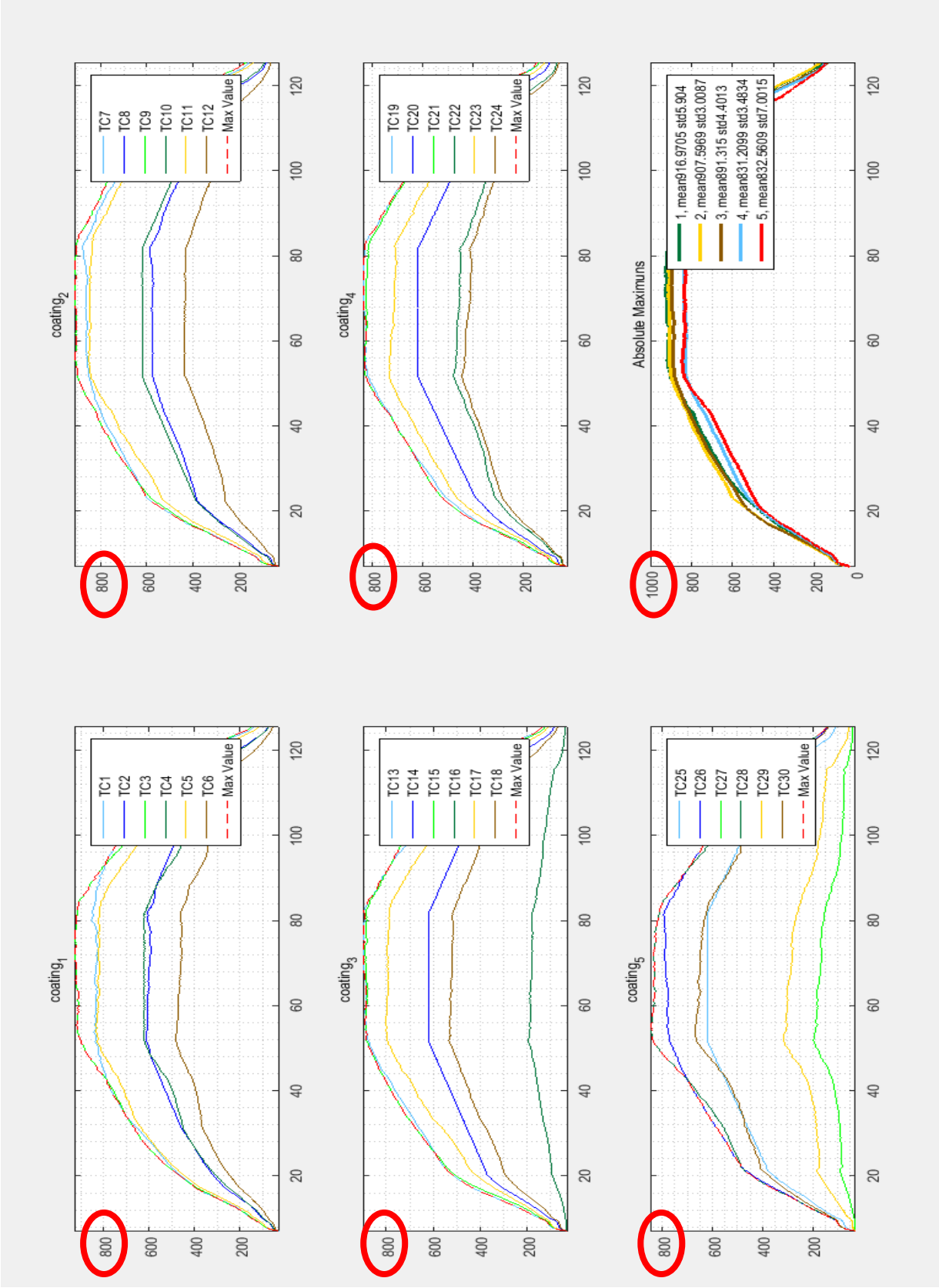


Figure 25: Real data obtained by re-testing all the samples with the second thermocouple configuration.

This confirmed a systematic overheating of around 200 °C over the maximum temperature in all the previous cycles and coating types. These results were immediately reported to the partners, and they decided not to continue with the test campaign, but to apply all the necessary measures to correct the test bench deficiencies and proceed with the second experiment campaign. Experimental and laboratory data were discarded for publication.

The longitudinal thermocouple configuration was chosen for the second campaign, and all the back wall thermocouples were removed.

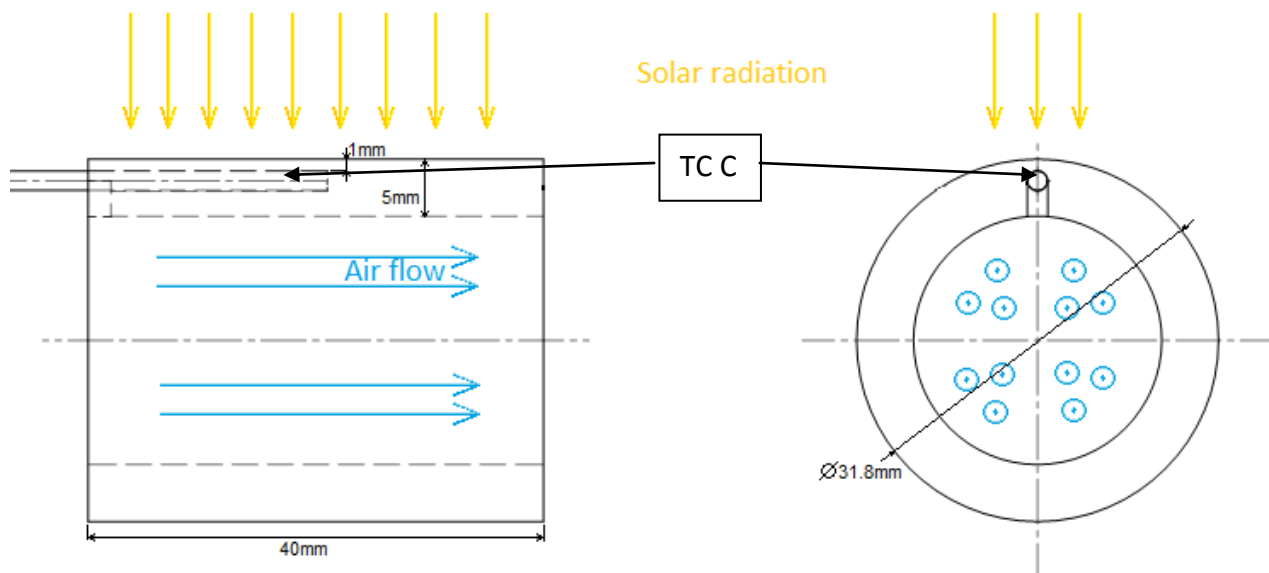


Figure 26: Detail of final thermocouple configuration.

4.4 Data analysis software

Raw data generated by the test bench during test cycles are treated and analyzed by an external routine written in MATLAB. The main goal was to summarize and report test data into key statistical indicators and charts in order to ensure experiment's traceability and to enable the researchers to evaluate and track at simple sight the record of thermal cycles. Every cycle has its own set of figures, generating an "Experiment Logbook".

In addition to the set of figures, the program also creates a file with key data about the cycle, such as the average temperature seen by each sample and the blower power for each coating line during the stationary part and the total cumulated radiation along that cycle. This key files are later included in a master file that crosses the testbench data with the laboratory optical characterization results helping the researchers to evaluate and track degradation patterns.

As mentioned previously, the testbench comprises two control loops: first one related to the flux control, and second one related to sample's temperature control. Parameters affecting the flux power are:

- Direct Normal Irradiance (DNI, W/m²)
- sample's focal distance (expressed in mm, with respect to the dish focal distance f)
- Reflectivity of concentrator (assumed constant, 92%; soiling neglected)

This, together with flux distribution maps, will enable further flux estimations. DNI readings are taken from a high precision pyr heliometer belonging to the facility's weather station (which is located about 100 away from the testbench). The testbench itself has its own additional sun sensor, calibrated with respect to that pyr heliometer. This sensor provides additional redundant data, in case of local cloud passage over the weather station. Test bench position is provided by its built-in linear drive encoder.

Following figures show typical data over one arbitrary cycle:

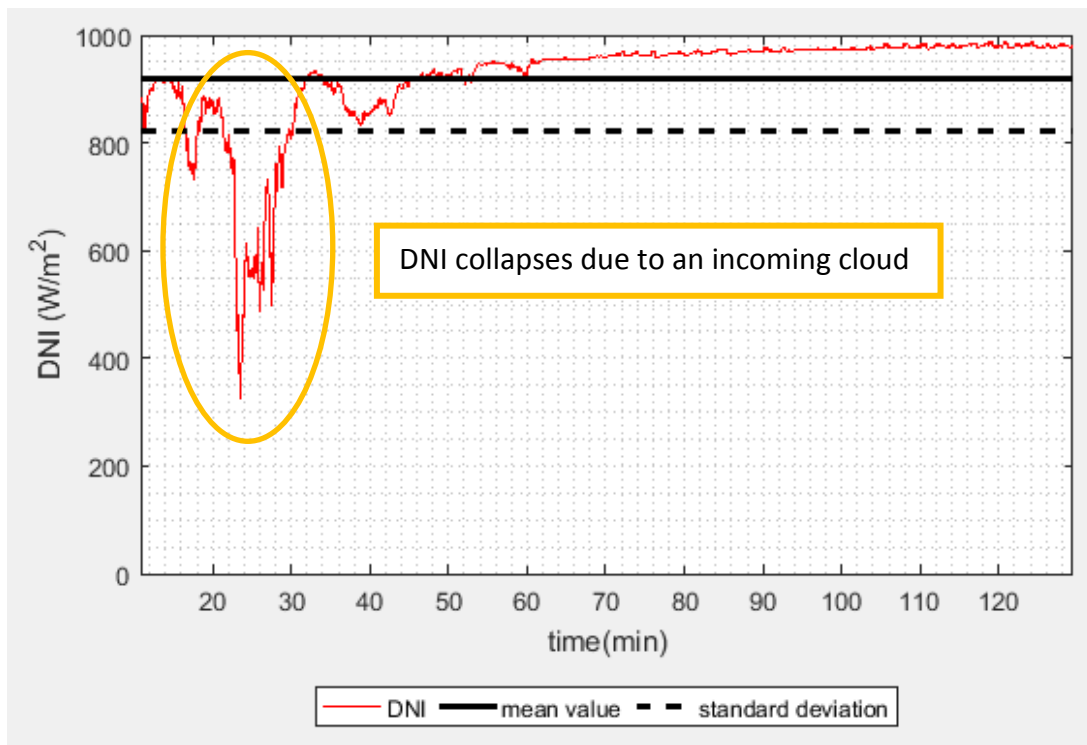


Figure 27: Example of DNI readings along an exposure cycle.

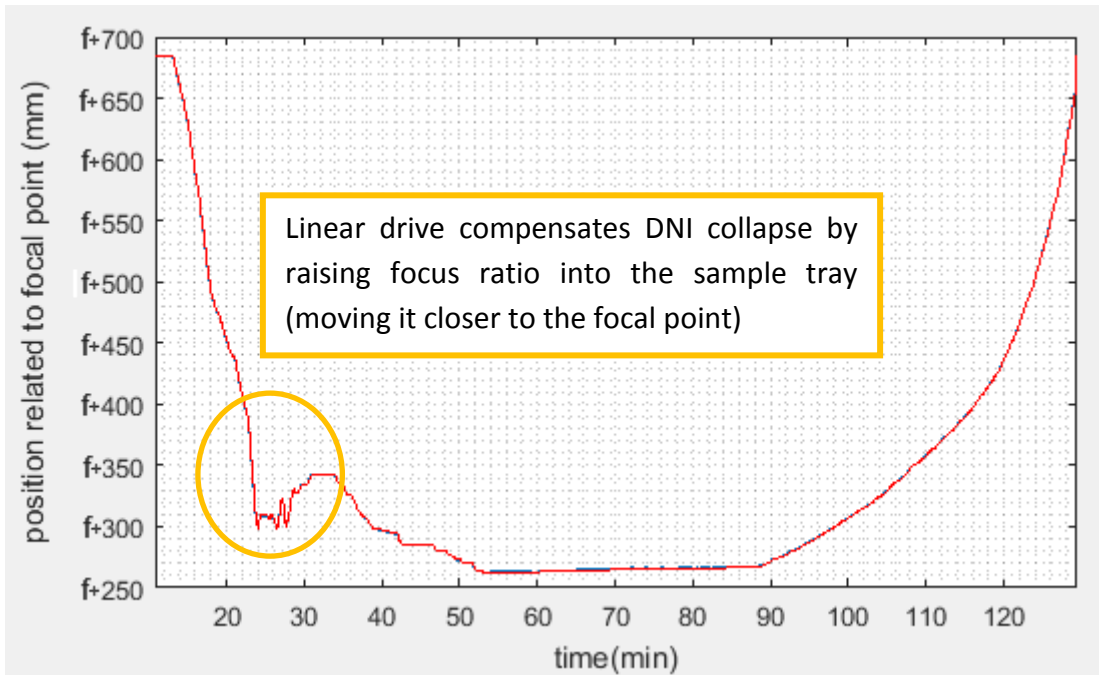


Figure 28: Example of focal distance evolution along an exposure cycle

The radiation flux on the sample's window is estimated by inputting DNI and encoder readings into the numerical flux model based on ray tracing techniques:

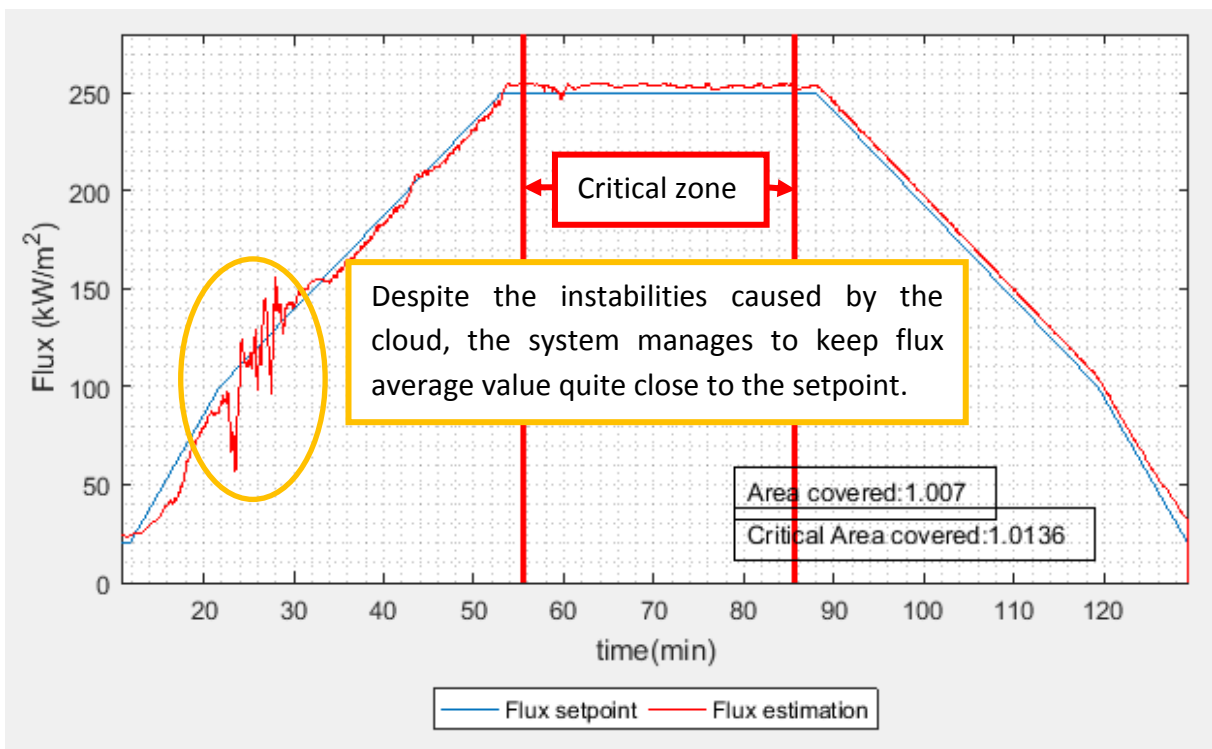


Figure 29: Example of Flux evolution during an exposure cycle

The area covered by this estimation (red) is related to the area covered by the set point curve (blue). This represents a “coverage factor” (applied dosi over intended one). A value of 1 means that the amount of radiation put into the sample window along the cycle was exactly the intended one. Values below 1 usually mean the presence of clouds or some kind of missadjustment in the linear drive producing a deficit in the solar flux dosis. Values above 1 usually means control loop misalignments. Timeframe between minute 55-85 (indicated with red vertical bars) is called cycle’s critical zone.

Regarding the temperature control loop, several data are plotted together in search for patterns. Thermocouple data is packed by coating type in order to compare temperature readings of equivalent sensors in different samples within the same coating type:

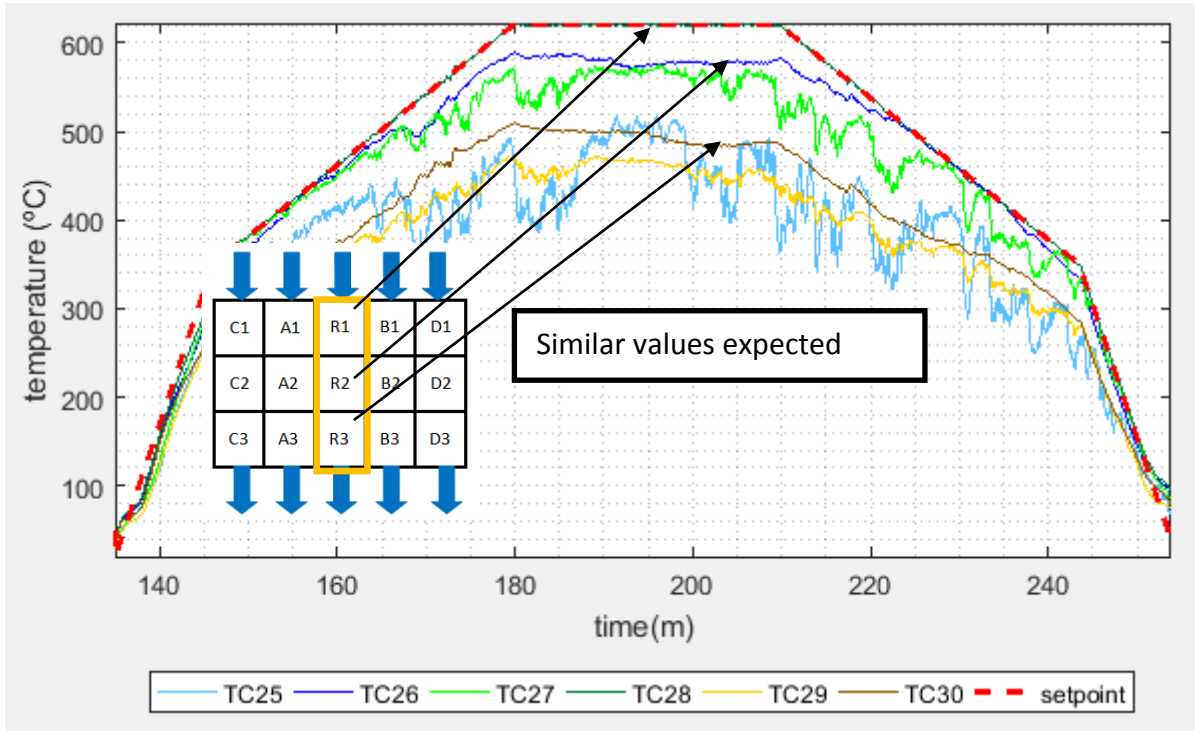


Figure 30: Typical thermocouple readings on the reference family during cycles 1-40 of campaign 1

Figure represents temperature readings of the three Reference (R) samples. TC 26, 28, 30 are assembled as TCA showed in figure 15. TC 25, 27, 29 are assembled as TCB of same figure. The front wall is irradiated with concentrated solar radiation, the rear wall is facing the ceramic insulation. The readings within each of those thermocouple groups should be theoretically very close to each other, since the incident flux was expected to be quite homogeneous along them and they all share the same blower channel. However, as might be observed, temperature offsets up to hundred degrees are detected between equivalent thermocouples mounted on different samples.

These particular data is what motivated a further research related to flux characterization and cooling mechanisms. Following figure shows temperature readings comparing equivalent thermocouples along different coating types:

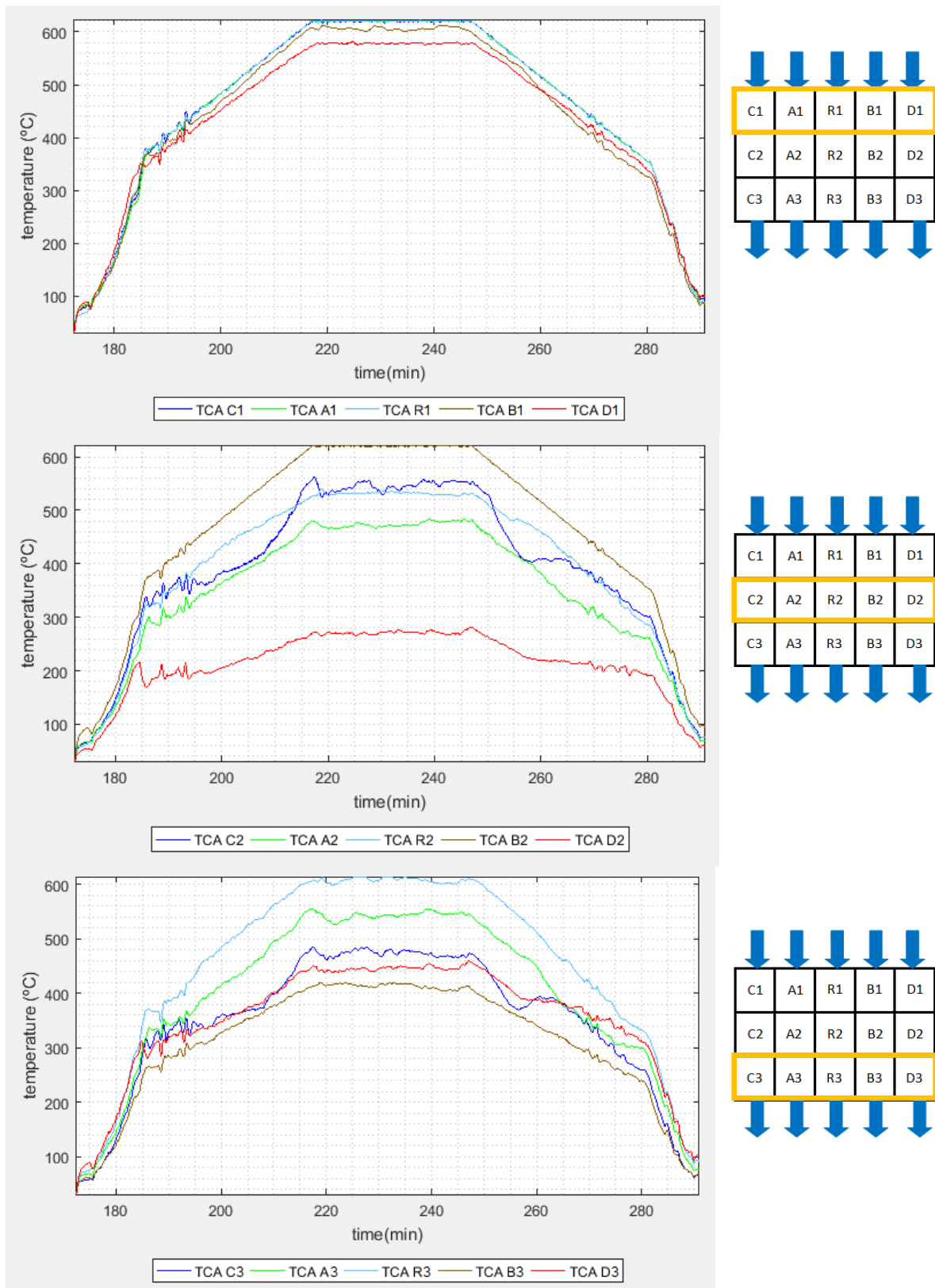


Figure 31: Horizontal comparisons of front wall thermocouple readings during cycles 1-40 of campaign 1

Temperature offsets show an evidence of horizontal temperature inhomogeneities, that can be motivated by either flux inhomogeneities or cooling gradients across the vertical direction.

Blower power is also monitored, since it is an indicator of systems' effort to evacuate the heat produced by the incoming radiation:

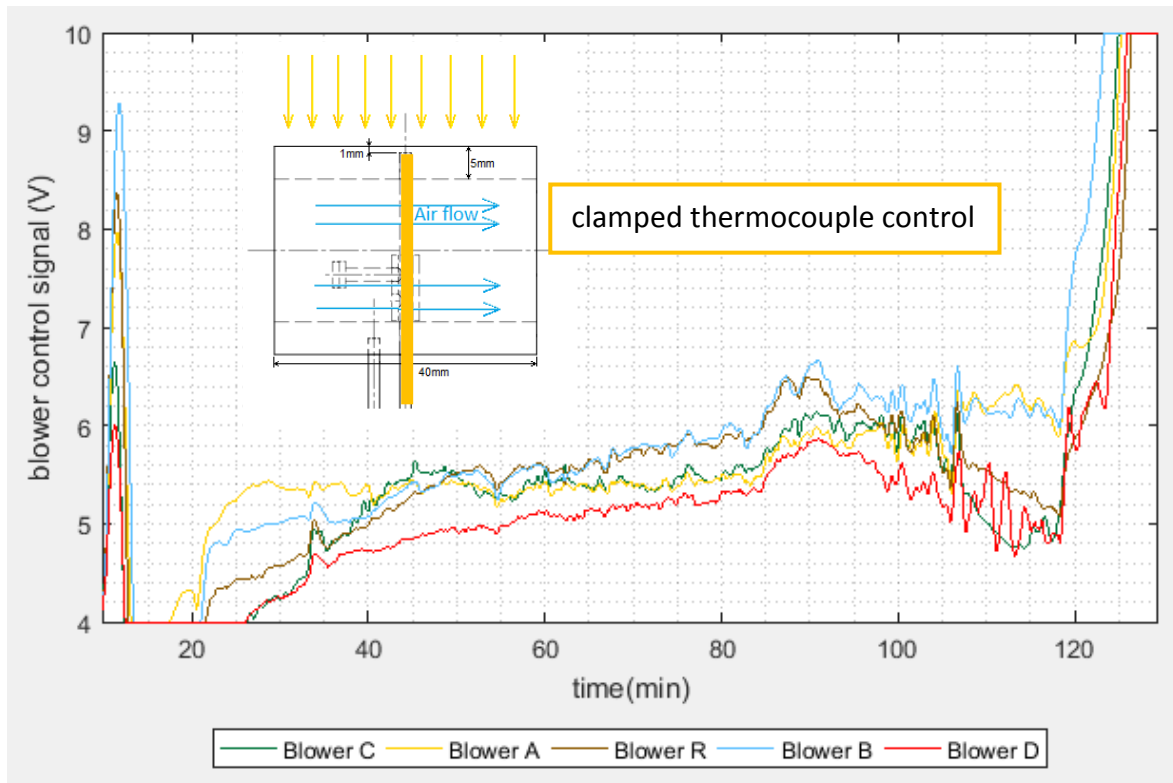


Figure 32: Example of blower control voltage signals along 1st campaign cycles 1-40, with clamped thermocouple configuration.

This plot is used as an indicator of how much effort is putting each blower into keeping it's row's maximum temperature under control (620°C setpoint for the critical zone). **Differences in blower power levels either mean transversal gradients in flux density across sample lines, or differences in the way temperature readings are being collected (faulty thermocouples).**

Since campaign 2 included longitudinal thermocouple control within the temperature control loop, it can be appreciated how average blower effort significantly rose to keep samples' wall temperature below the setpoint value.

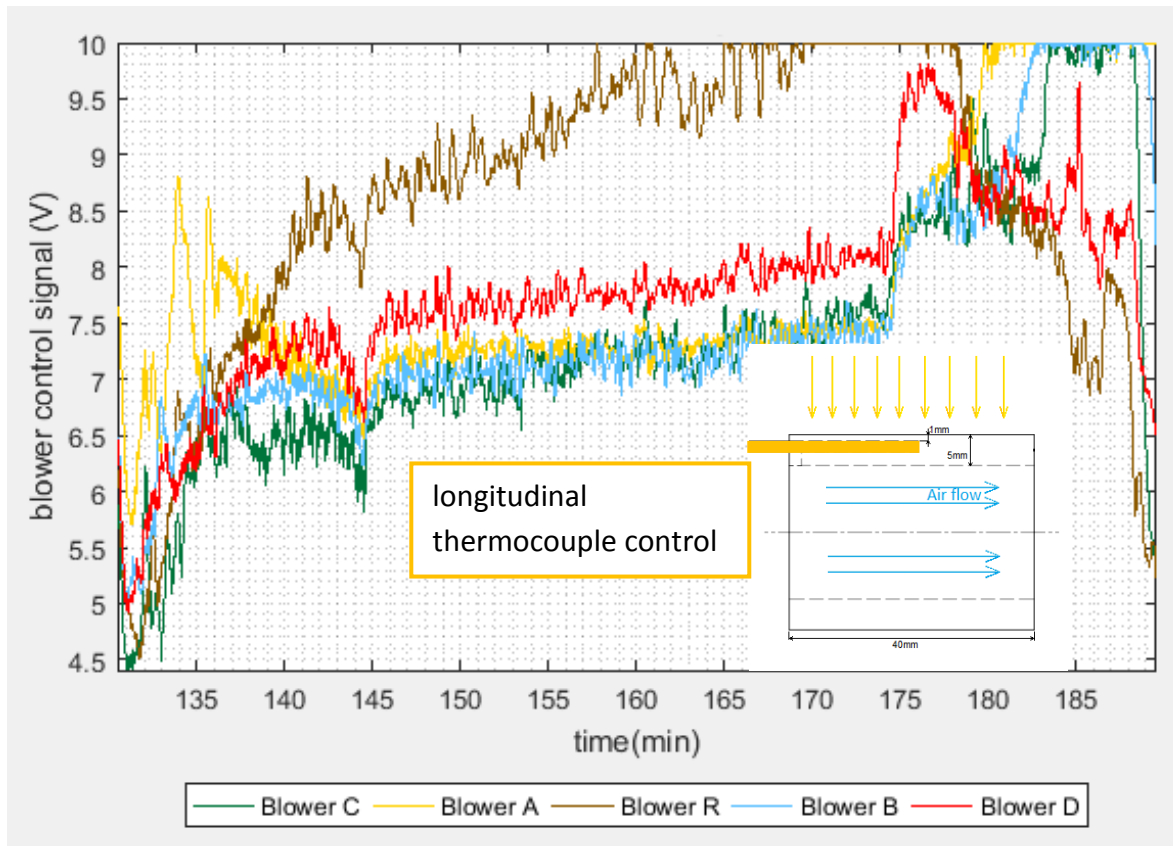


Figure 33: Example of blower control voltage signals along 2nd campaign cycles, with longitudinal thermocouple control.

Notice as well how in this case blower R gets saturated and it is no longer able to keep temperature under control even working at full power. In order to prevent this from happening, small rectangular area on the mirror was covered with tape, passively reducing the local reflectivity flux on line R.

The longitudinal thermocouple assembly was selected for second campaign test.

By using these new thermocouple configurations for the temperature control loop, the air blowers worked, as expected, at a higher average power than on the test performed during the first campaign.

In addition to these plots, the program also calculates the radiation dosis (energy) received by each sample during the exposition cycle. This however is a process that requires deeper understanding of the solar flux distribution, and therefore will be adequately covered in the next chapter.

4.5 Experimental Flux Measurement: CCD Method

In order to get an experimental pattern for the flux maps distribution, a new setup was introduced in the test bench. A CCD grayscale 12-bit resolution camera (Baumer TXG14 with Nikon adjustable tele-objective 70-120 mm and Grey Filter strength 7) was installed at the center of the dish and a new 1x1 meter ceramic lambertian target without window was installed over the sample tray. Process followed at this point was as explained in chapter 0

Two different image sequences were taken:

With the Distal focused, the first one consisted on a set of 17 grayscale images of the sample tray between positions f+235 to f+390. Each photo is 12 bit pixel-deep in resolution.

Later on, the **unwindowed ceramic target was installed over the sample's one**, and another set of images was taken. Offset between sample tray and the new unwindowed ceramic plate was 60mm. Therefore images of the second sequence were taken 60mm farther than those of the first sequence in order to compensate assembly's offset. The goal of this operation was to enable exact pixel correspondences between sample positions and experimental flux readings. This will be deeply explained in the following pages.

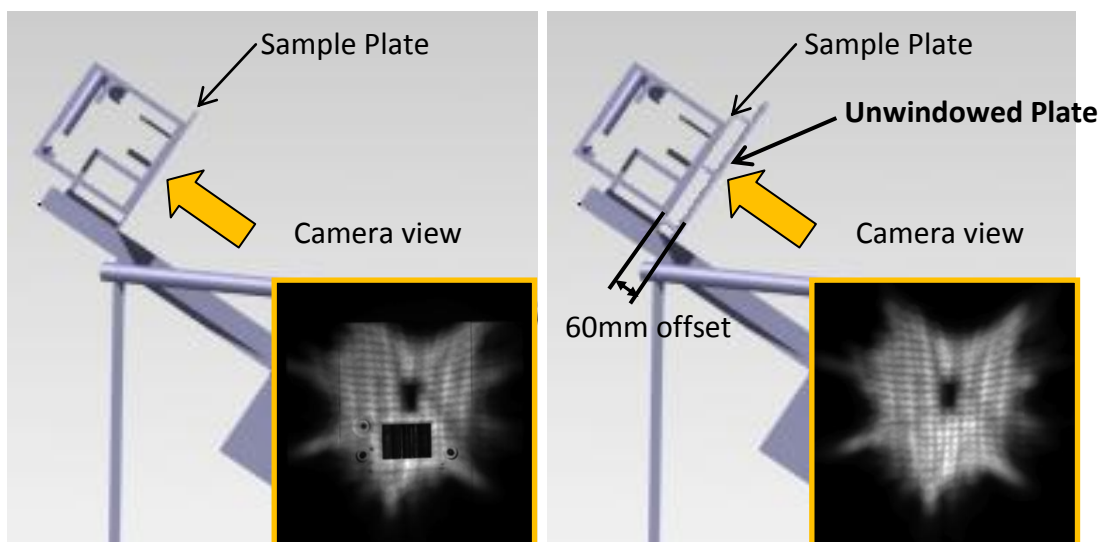


Figure 34: Example of flux patterns observed on the sample tray (1st image) and the additional unwindowed plate (2nd image) in this case both images represent flux footprint at f+390mm.

Some of the results can be observed in the following table. Complete image sequences are plotted in the appendix at the end of this document.

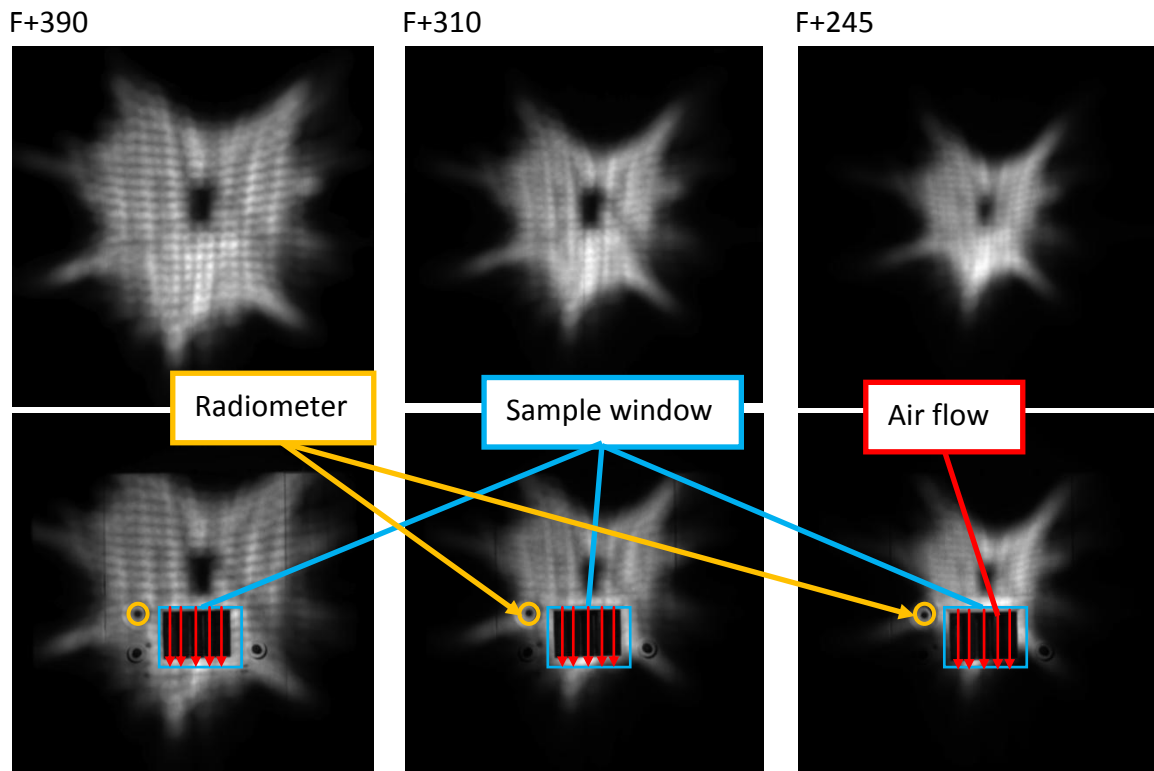


Figure 35: Equivalent images of the first (below) sequences and second (above). Samples and radiometer can be appreciated in first sequence images. Raw flux distribution is shown in the second sequence. F+390 means relative distance 390mm further from the Dish optical focal point.

At this point, a family of 17 pairs of images was obtained, each pair taken at equivalent focal distance and containing one image of the flux pattern and another one with the sample plate. Our aim is to **identify sample locations on first sequence images and calculate the incident flux on those same locations** using the images of the second one.

However, before doing that, every raw image has to be digitally treated. All the images showed in this document up to now have been actually *post-processed*. Raw images include apparent deformations produced by the misalignment between the camera axis and the ceramic plate and therefore, they're cropped, flattened using a geometric transformation (homography) and rescaled to 1000x1000 pixel 12 bit depth using a bicubic interpolation. Finally, the background noise signal is removed in order to have a zero value background (otherwise there would be calculation errors in the next steps).

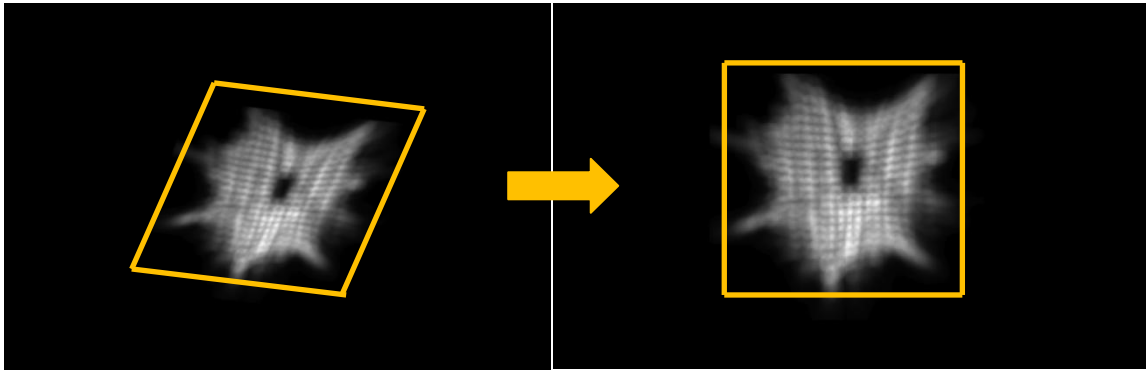


Figure 36: Left) raw image. Right) raw image after homography. Left image deformations have been exaggerated in order to make them noticeable.

Experiment consistency was checked. Since all the sequence's photos were taken with the exact same camera settings (exposure time, gain...), the only remaining parameter affecting them is the focal distance at which each one was captured. It seems reasonable that the overall "energy" contained in each image should remain constant for all of the images, just more or less dispersed depending on the focal distance, (always considering that all radiation reaches the target without spillage losses). That can be checked by **adding up all the pixel gray values within each individual image** and checking how much the results differ along the image set. By doing so, only a 1% total power variation was observed within 13 out of 17 images. The 4 farther images from the focal point shown total "gray power" 5-12% below the expected value, but this is due to the fact that these images were taken so far from the focal point that a portion of the flux was actually reflecting on the aluminum frame around the Lambertian target instead of doing it on itself.

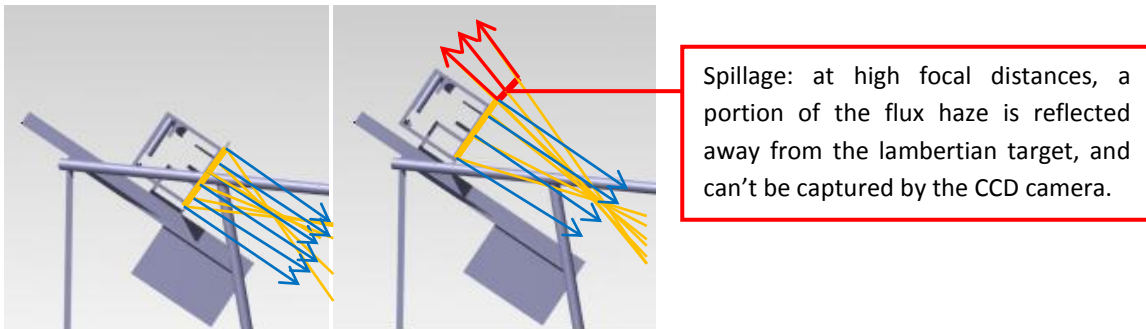


Figure 37: Comparison between non-spillage and spillage situations.

By having a flux distribution map we can now calculate the average flux affecting each sample. For that, first we must know the sample's position related to the flux distribution maps. We can find it out by looking at the first set of images:

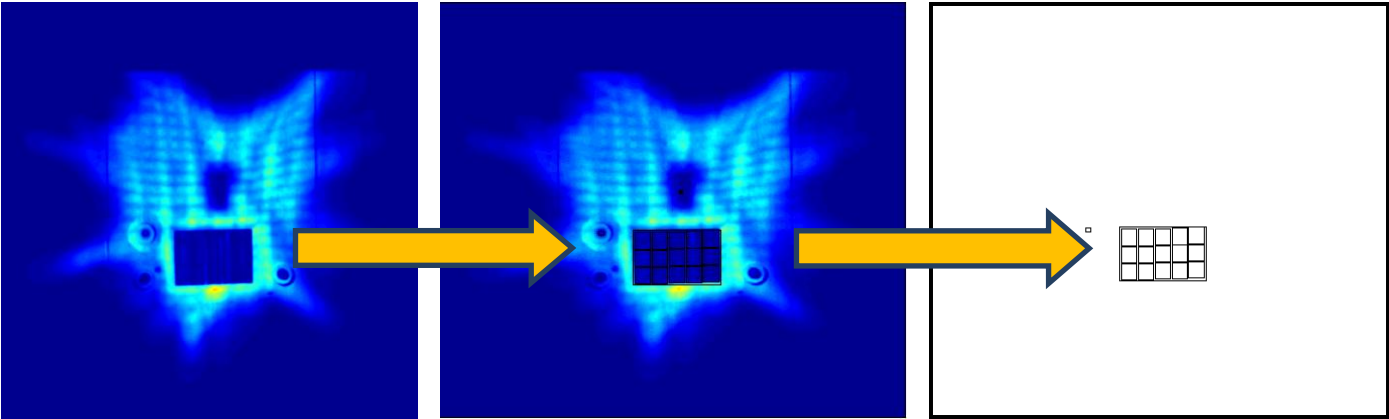


Figure 38: Step 1: extracting sample's position grid from raw CCD images

And then apply the location pattern to the flux map:

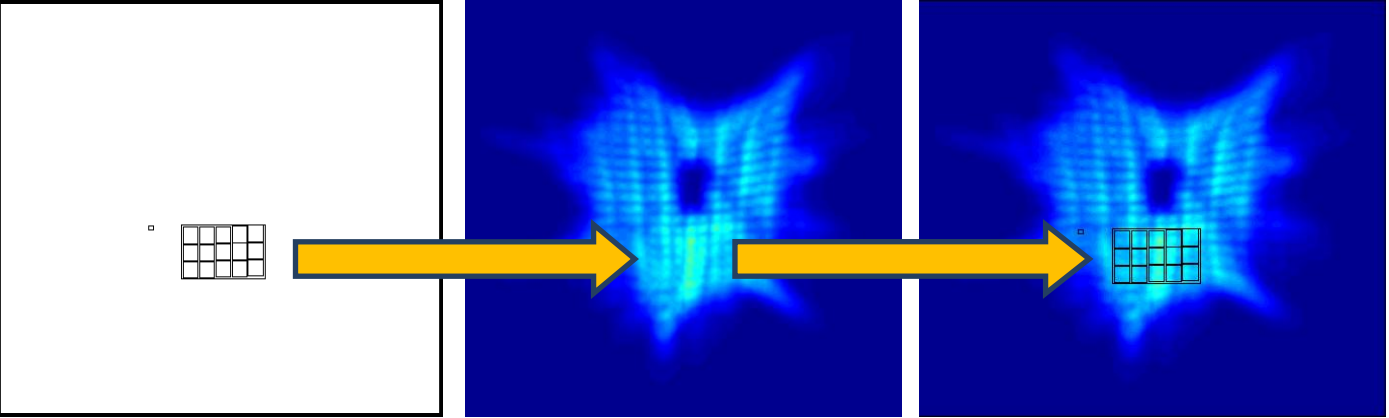


Figure 39: Step 2: applying sample's position grid to the flux maps

Once the correspondence between the flux pattern and the sample's location is established, we can track flux dosis on each sample by calculating pixel's average values on the equivalent area on the flux pattern:

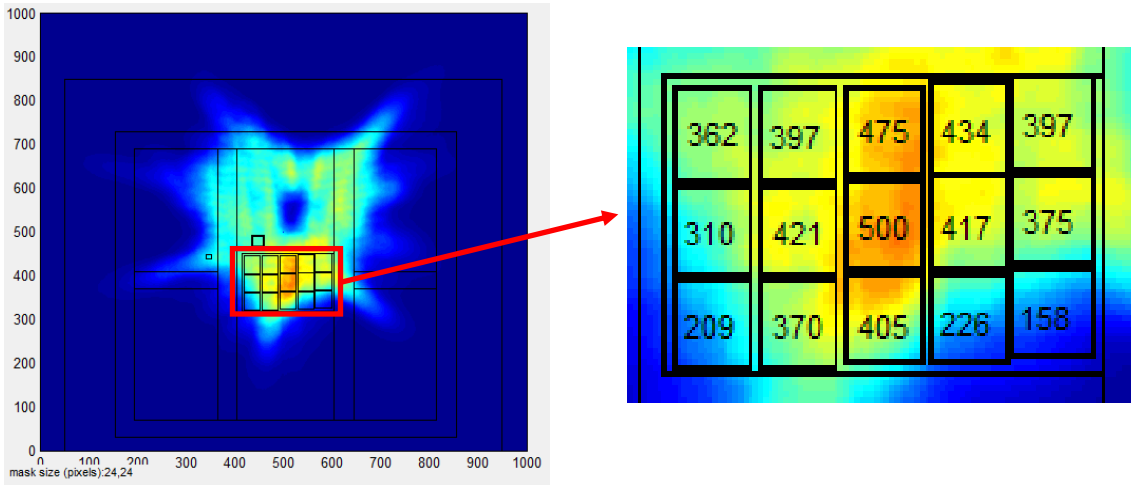


Figure 40: Flux values in kW/m² for all the samples at focal distance f+275.

By doing so on all images of the sequence, a flux curve for each sample was obtained, expressing total received flux power as a function of focal distance for each of the samples:

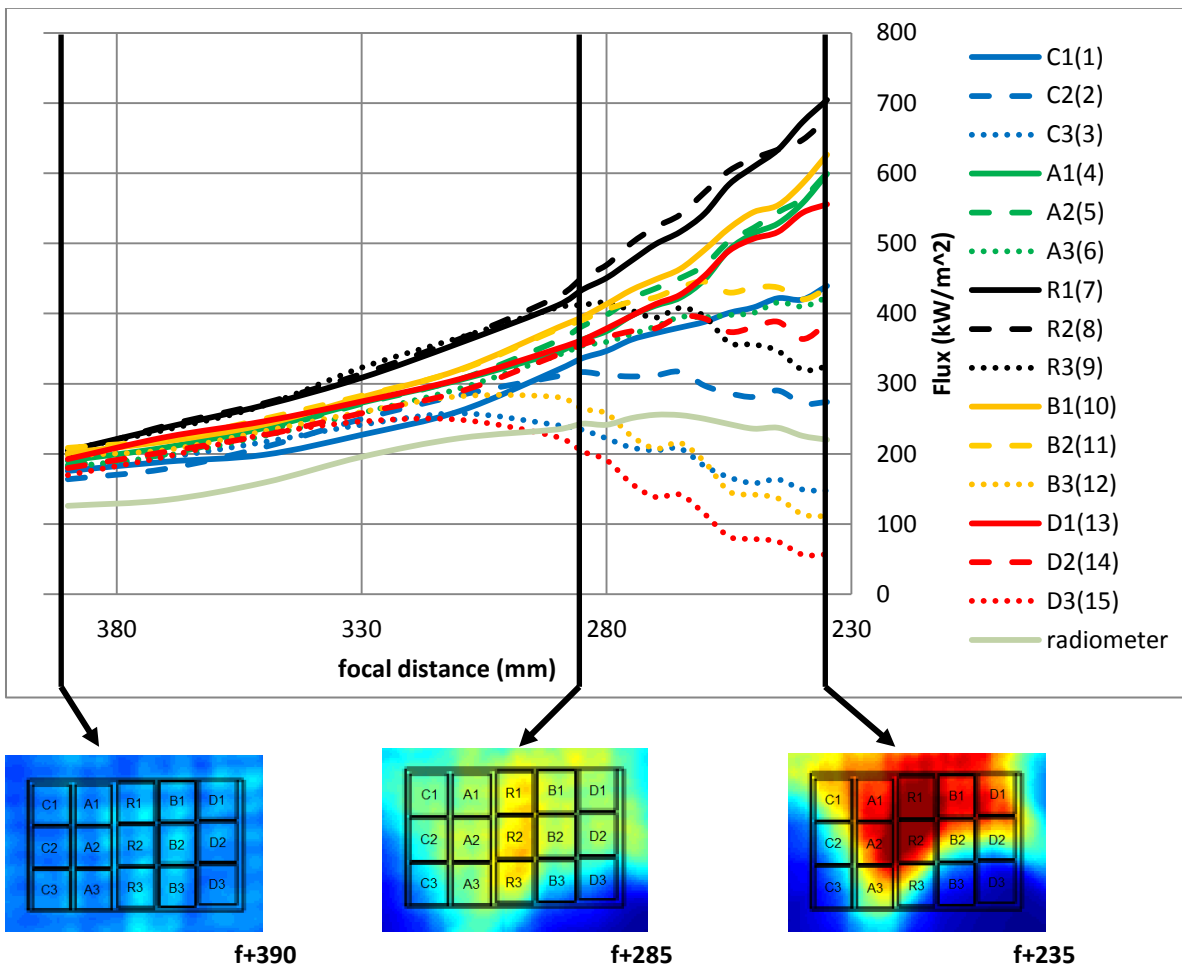


Figure 41: Modeled average flux on each sample (and radiometer) as a function of focal distance

This flux curves can later be used for calculating the total flux dosis along a complete exposure cycle by just integrating them stepwise in time.

4.6 Experimental Flux Measurement: Flux Map calibration

In chapter 3.4. it was concluded that further Flux Map calibration was necessary in terms of reaching enough accuracy for the data. This was tried by installing a radiometer on a carefully selected location in our sample tray aiming to collect data that could be later extrapolated to the rest of the Flux Maps



Figure 42 external appearance of the CAPTEC radiometer

Several locations were considered basing on available flux maps data. Desired criteria for this were areas in which radiation curves were smooth and continuous, with nearly linear increase, if possible. Maximum and minimum values within these curves should also be kept inside instrument's limit specifications. Some of the regions were also discarded due to interference with the supporting frame underneath:

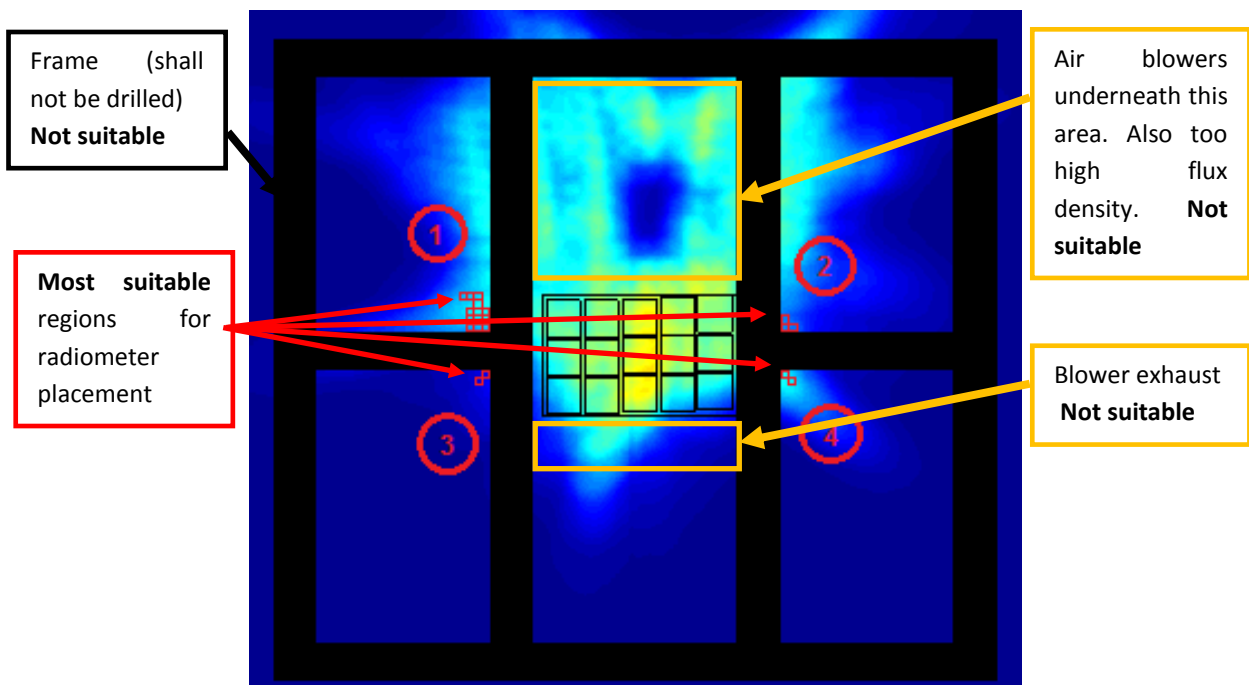


Figure 43: Analysis for radiometer placement

Four regions were identified for suitable radiometer location. Using the available flux maps, a survey was made on these regions to identify the 10x10mm spot with the best flux curve according to our criteria. Following figure shows some of the analyzed locations and their respective flux curves:

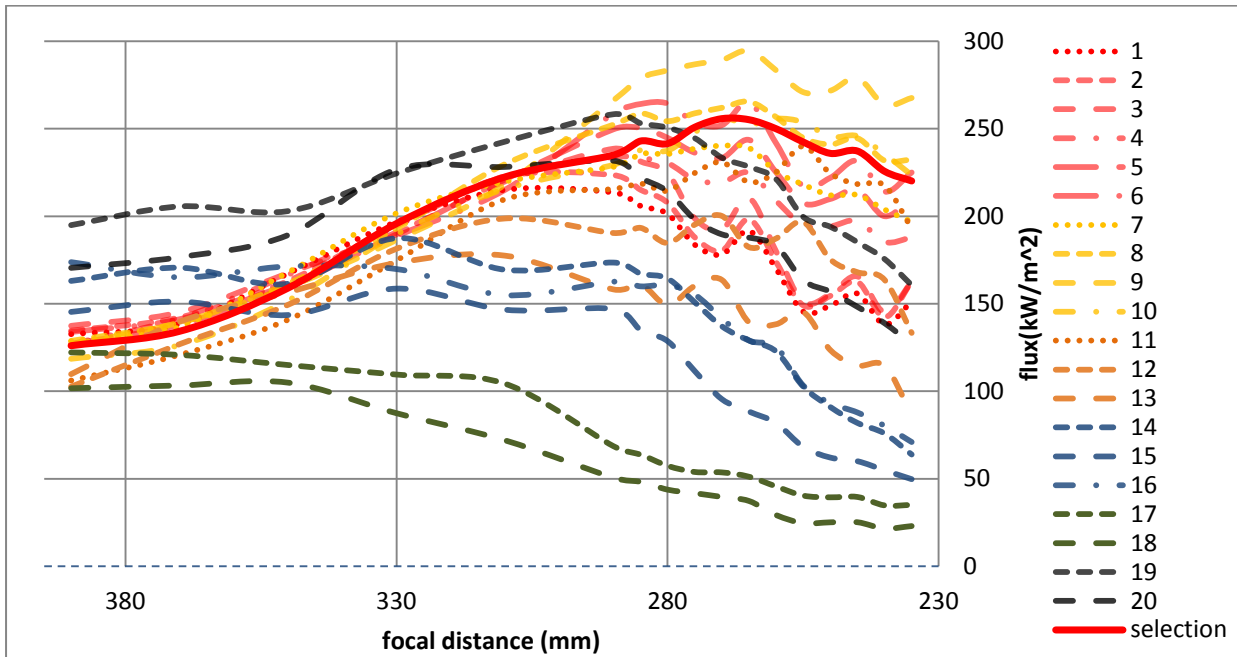
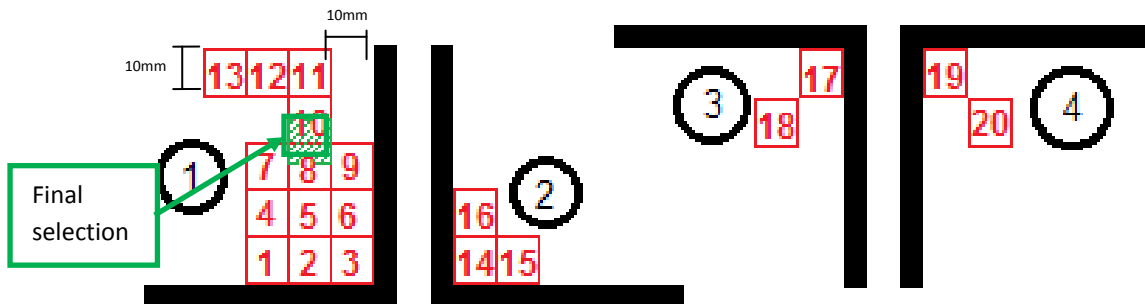


Figure 44: Considered locations for radiometer placement and calculated flux curves for each of them.

Final selection was a 10x10mm square 25mm separated from the bottom frame and 10mm separated from the side frame. Its flux curve according to the flux maps is marked in solid red on the figure.

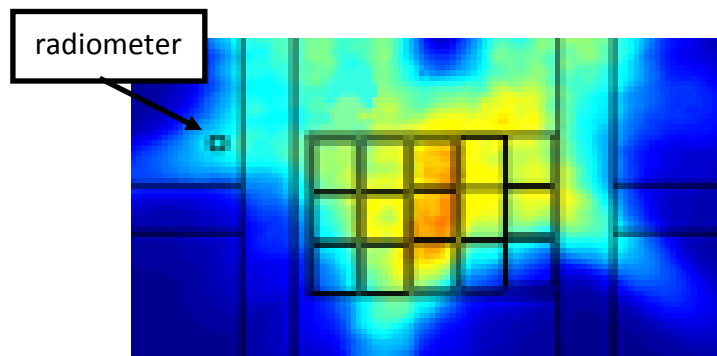


Figure 45: Detail of radiometer location within the flux map.

The radiometer [24] is a customized under demand model from CAPTEC. Its sensing area has 10x10mm and specs indicate operation conditions up to 200°C and 500kW/m² of radiant flux. One of its biggest advantages over other options is a sampling rate of up to 10Hz, whereas market standard (Gardon gauges) is 1Hz. In addition to that, it has finer signal resolution and includes a built-in temperature sensor.

The instrument must be water cooled. Basing on the available flux map data, it was calculated that an “off the shelf” computer water cooling system would satisfy the cooling requirements by a generous margin. The component disposition is as following figures show:

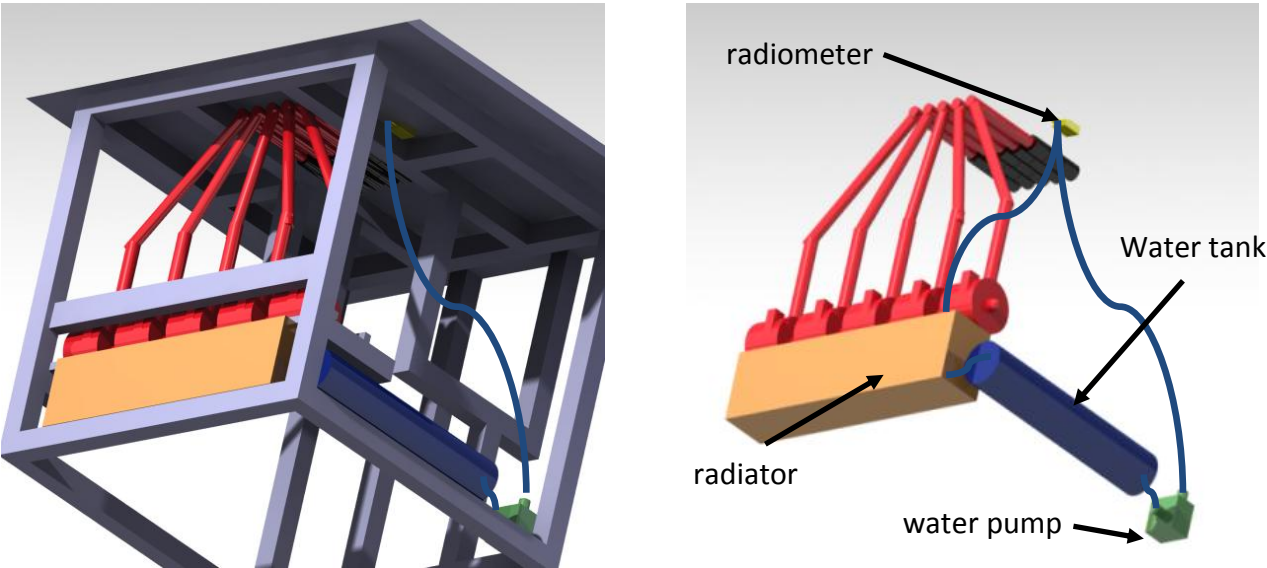


Figure 46 Detail of radiometer location within the test bench’s frame

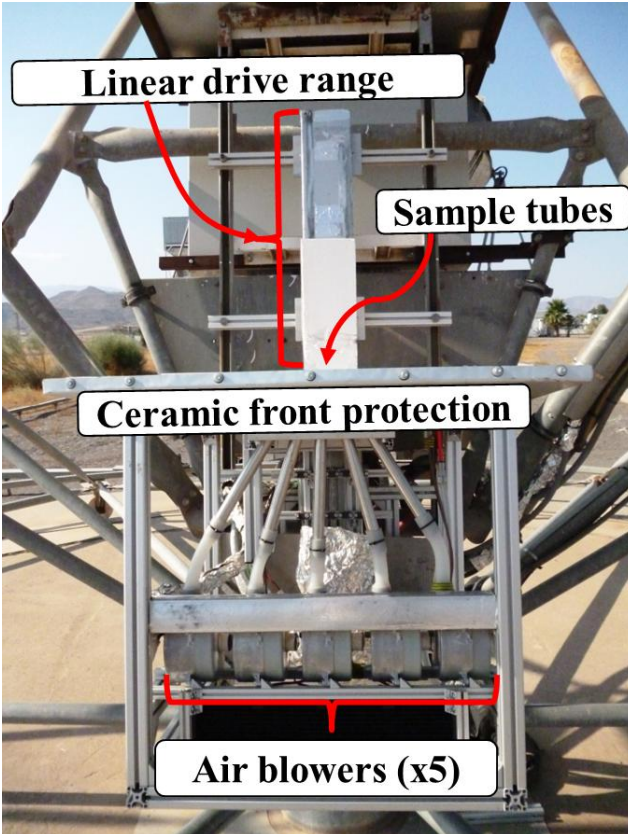


Image 4: Image of the testbench

Once the radiometer was installed, readings started to be taken during regular test cycles. Following figure compares radiometer readings collected along 1 cycle with the expected flux level estimated according to the flux maps developed by the CCD method.

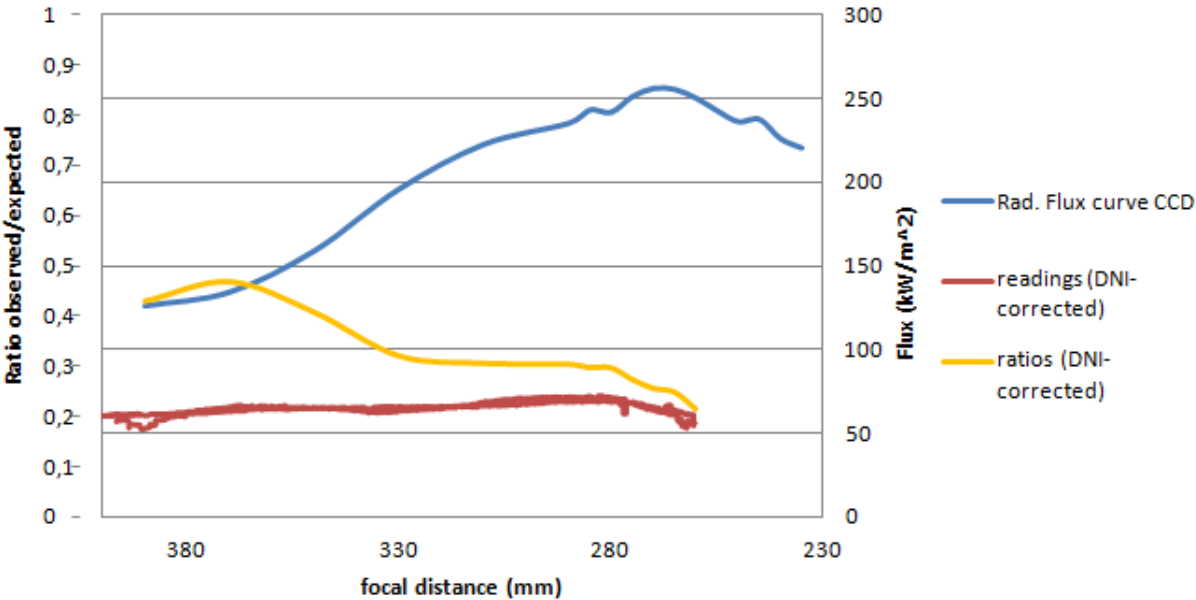


Figure 47: Comparison between measured and expected flux readings along different focal distances.

Readings are shown corrected by DNI data in a way that both blue and red curves can be straightforward compared. As it can be noticed, radiometer readings are much lower than expected and show no progression to rising solar concentration rates. This lead us to think on somekind of sensor malfunction or possible calibration errors. Ratios between measured and expected readings are also non-constant along the focal positions (yellow line), except for a narrow interval between 235 and 335mm. This fact makes it unlikely to be a matter of calibration or signal interpretation, since the error ratios would be in both cases expected to have a flat shape along focal positions (lets remember that according to manufacturer specs, output signal is proportional to flux). Sensor malfunction or somekind of unexpected interaction between components were considered the most probable reasons for this issue. In order to make a better guess of what could be happening, we also cross compared the readings of the radiometer’s built-in temperature sensor along that same cycle:

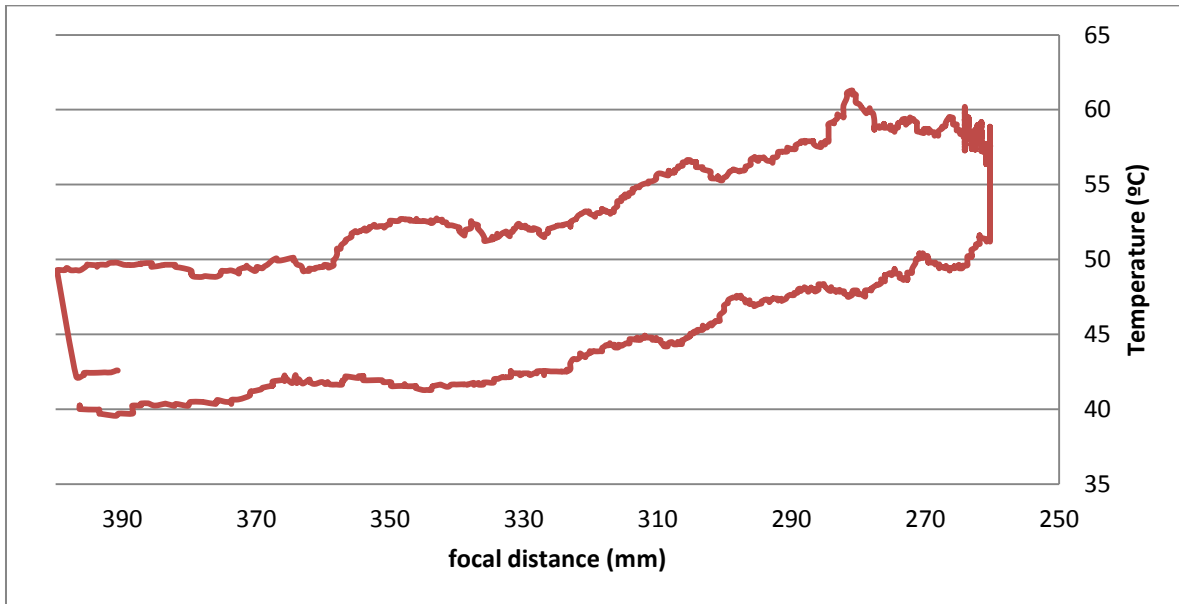


Figure 48: Radiometer temperature readings along cycle exposure during test campaign 2

This time, a rising temperature progression can be noticed when getting closer to the focus, so it can be proved that the instrument was being at least partially exposed to the solar beam. Strong hysteresis can be noticed between cycle's warm up and cool down phases. This seems reasonable considering the high volume of water contained in the radiometer's cooling system.

Because of work schedule, efforts on this topic were abandoned at this point. Still further steps were conceived to be taken when all the other priority tasks were completed. One idea was to replace the CAPTEC radiometer with a previously tested Gardon one, and repeat the test so that it could be dismissed if it was a component problem or an external issue. Performing external calibration of the CAPTEC was also considered, but the PSA's calibration team could not guarantee precise calibration on this model because their facilities and methods were quite specialized for Gardon ones.

4.7 Experimental Results: First Campaign

Spectrophotometer measurements were always performed on the same small area of 15 x 5 mm on the front side of each sample. A microscope image of that area was taken as well. Lastly a regular image at real size scale is taken to see the overall appearance and degradation state of the samples. This process was performed at cycle number 0 and repeated every 10 cycles.

Here is a table showing the progression of one of the samples, in particular sample C1. The infrared spectrophotometer was not available during first campaign, and therefore IR emittance readings were unknown. Overall sample efficiency (eq. 8) couldn't therefore be either calculated.








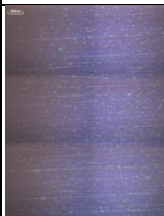





Cycle	0	9	20	30	40	50	60
Reflex image							
Microscope image	No image available						
Solar absorb	95%	93.4%	89%	88.6%	87.2%	87%	87%

Figure 49: degradation of sample C1 along campaign 1.

The above example was one of the cases at which the results were most confusing. As can be observed, the degradation of this particular sample (C1) is evident both in large and microscopic scales. This kind of degradation level and absorptance loss was totally unexpected in comparison to other accelerated ageing tests running in parallel. This motivated a revision in the test procedures.

The remaining samples however did not show such an evident degradation on their coatings. Still, their absorptance losses were significantly above 0.5%, which was as well out of original expectations. Because of the experiment deficiencies, detailed spectrophotometer data of this first campaign won't be reviewed in depth here. Second campaign data will do in the next chapter, showing interesting results.

4.8 Experimental Results: Second Campaign

Additional modifications were introduced during the second test campaign. First of all, camera and microscope settings were homogenized along all the rounds. This was in the first campaign discarded because priority was given to image quality (optimal light conditions and automatic white balance for each different sample). However, partners reported difficulties when cross comparing different sample's microscope and camera images and therefore it was decided to homogenize image settings even meaning losses in brightness or color resolution on some of them. Here is again a table showing the progression of C1 during campaign 2.







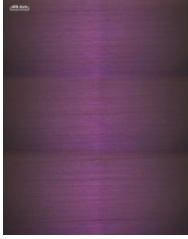
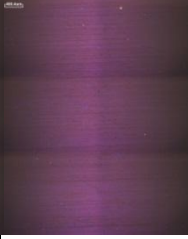
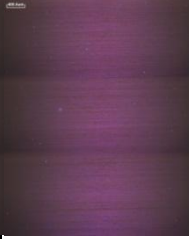
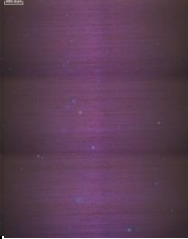
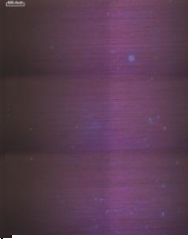
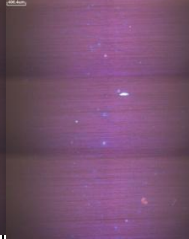
Cycle	0	20	40	60	80	100
Reflex image						
Microscope image						
Solar absorb.	94.8%	94.8%	94.8%	94.6%	94.8%	94.8%
Thermal emitt.	22.4%	24%	22.4%	22.4%	24.1%	25.8%
Overall efficien	91.1%	90.9%	90.8%	90.9%	90.8%	90.6%

Figure 50: degradation of sample C1 along campaign 2

Spectrophotometer data is worth to observe in detail this time, since it shows some key features that can help us to better understand coating behaviors.

Following figures show the spectral absorptance progression of the coatings in wavelengths 280-2500nm. First one represents data before any test was carried out, and second shows data at the very end of the test campaign. Data source is the UV-Visual spectrophotometer Perkin Elmer Lambda1050 [17].

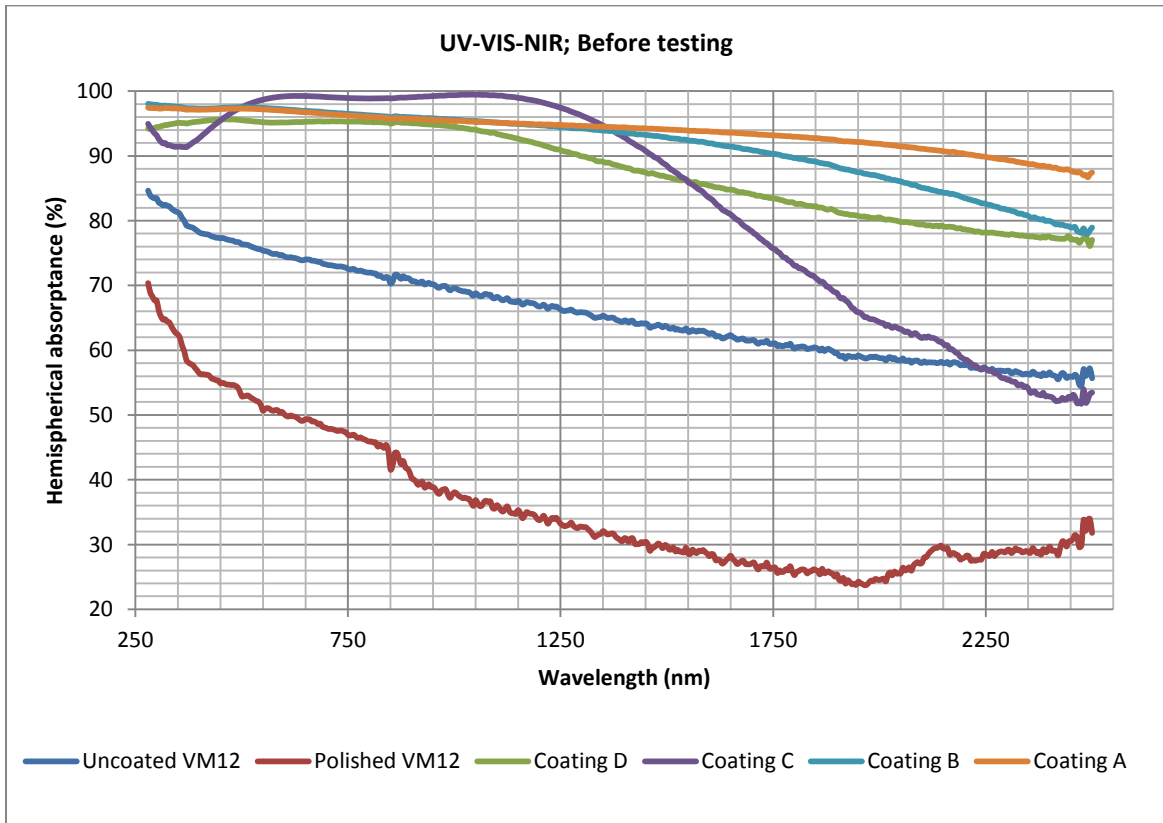


Figure 51: Sample absorptance ratios for UV to NIR wavelengths before the experiments

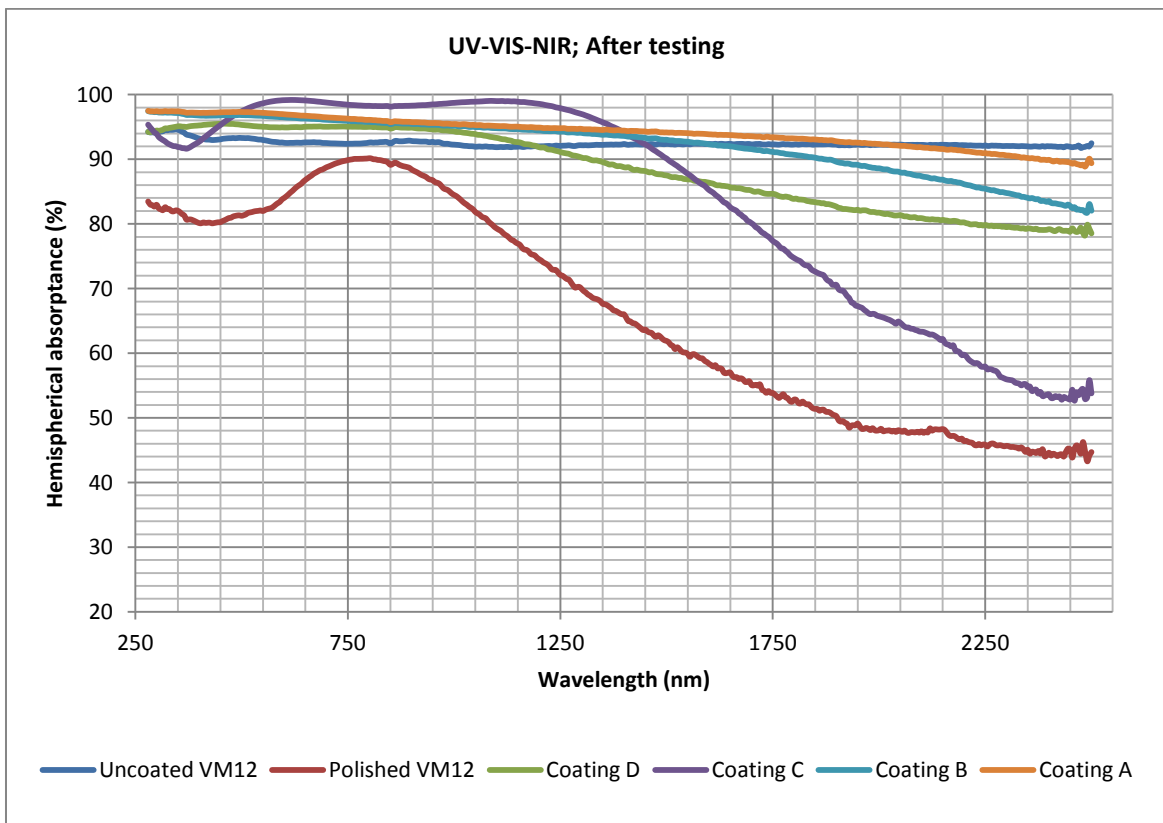


Figure 52: Sample absorptance ratios for UV to NIR wavelengths after 100 cycles on campaign 2

Besides dark blue and red lines, which respectively indicate raw and polished VM12 [21] surface (no coating), the degradation progression this time seems very low in all cases. These results however fit much better with the ones reported by our partners in parallel experiments (oven tests, without flux).

Dark blue and red lines show the behavior of the uncoated VM12 [21] metal surface (raw and polished). Their performance seems to get better in time, which might sound unintuitive but it is very reasonable taking into account that forming oxide and impurities during the degradation process contributes to block their natural reflectivity and improve their absorptance to a certain extent.

Lack of degradation indicates that it might be necessary to perform at least one more order of magnitude in terms of flux exposure time in order to reach noticeable degradation level and it doesn't allow either a clear correlation between it and the measured radiation dosis. Increasing the number of radiation cycles would however get in conflict with the original conception of the study, *Accelerated Aging of Solar Absorber Coatings*, since performing campaigns with 1000 exposures cycles wouldn't mean any *acceleration* at all.

Current considerations within the community suggest increasing flux dosis by several times to cover higher absorbed dosis in shorter time periods. This however implies escalation problems in terms of managing test bench size, number of samples able to be tested simultaneously and size of cooling systems that must be discussed within the research community.

5 Conclusion and Outlook

Biased thermocouple configurations during the first measurement campaign caused the discarding of experimental data. After the inter-campaign modifications, the test bench proved to be reliable enough to perform exposure cycles with almost no human intervention, highly capable of accurately keeping flux and temperature setpoints even in adverse or unstable weather conditions and capable as well to safely stop the experiments under unexpected sensor behaviors. In addition, despite flux inhomogeneities, CCD flux mapping together with the data software analysis allowed us to keep a very detailed track of the radiation dosis for each single sample and all the rest of the experiment parameters, enabling its traceability and reproducibility.

The CCD method use to measure spatial distribution of solar flux turned out to be really satisfactory, enabling us to calculate reasonably accurate 3D models of the flux distribution rates within our sample tray and keep track of radiation dosis applied on the samples every cycle. Still, even having a detailed model of the flux distribution rates within the tray, it is important to remark that further improves are still to be applied specially to radiometer behavior and radiometer data extrapolation into the flux maps. Still, it was demonstrated that usage of hybrid methods (direct and indirect) while performing flux measurements on concentrated sunlight radiation can provide high quality data in terms of depth and spatial resolution at a much reasonable cost compared to other ones (only required hardware is a camera, a lambertian target and one or two radiometers). Still, our experiences at this regard show radiometer-CCD data correlation is very sensitive and could generate unaffordable errors when poorly done and in the absence of previous estimations or reference values, having a second radiometer for data redundancy could be a must in terms of gathering reliable scientific data.

Further trials must be done in order to reduce radiometer's data uncertainty and to improve the reliability of absolute flux values. The radiometer performance was definitely set to be improved before considering its integration into the flux control loop. Further instrument calibration would be desirable, and data reading fluctuations motivate a review in its positioning.

In terms of degradation, the sensibility to overheating of selective coatings (or polished surfaces) was made patent. Non selective coatings proved to better hold out of range temperatures, which should also be taken into account if accidents or plant malfunctions are to be considered. Still, the available data, including oven tests performed by other research groups, suggest temperature levels and cycles as the main mechanism for coating degradation, relegating direct radiation effects to a secondary plane in terms of importance. Detailed contribution of radiation dosis to degradation rate could not be analyzed, since even being able to accurately track radiation dosis on each sample, these seemed to be at least one order of magnitude below the minimum required to start appreciating any degradation on them at all.

This forces to reconsider the original experiment design in order to model long term degradation processes with short term experiments.

Bibliography

- [1] Lazard Inc.: *Levelized Cost of Energy Analysis 2017*. 2017. [Online]. Available: <https://www.lazard.com/perspective/levelized-cost-of-energy-2017/> [Cited in 2017].
- [2] C.Kost et al.: *Levelized Cost of Electricity*. Fraunhofer ISE, November 2013.
- [3] D. Z. f. Luft-und-raumfahrt: *AQUA-CSP Concentrating Solar Power for Seawater Desalination*. November 2007 [Online]. Available: http://www.dlr.de/tt/desktopdefault.aspx/tabid-3525/5497_read-6611/ [Cited in 2017].
- [4] Innogy GmbH: *Andasol 3 Solar-thermal power plant*. [Online]. Available: <https://iam.innogy.com/en/about-innogy/innogy-innovation-technology/renewables/solar-energy/solar-power-plant-andasol-3>
- [5] National Renewable Energy Laboratory: *Parabolic Trough Projects*. [Online]. Available: https://www.nrel.gov/csp/solarpaces/parabolic_trough.cfm [Cited in 2017].
- [6] Solenix GmbH: *Parabolic through field*. [Online]. Available: https://static.construible.es/media/2016/12/0906_andasol.gif
- [7] Torresol Energy SA: *Solar Tower*. [Online]. Available: <https://i.pinimg.com/originals/fe/eb/6c/feeb6c9d68462f0edc7a35ebfa37952f.jpg>
- [8] W. Beckman. J.A. Duffie: *Solar Engineering of Thermal Processes*. Hoboken, New Jersey: John Wiley & Sons 4th ed, 2013.
- [9] William B. Stine et al.: *Central Receiver Systems*. [Online]. Available: <http://www.powerfromthesun.net/Book/chapter10/chapter10.html>
- [10] NewEnergyUpdate: *ACWA Power scales up tower-trough design to set record-low CSP price*. New Energy Update, 2017. [Online]. Available: <http://newenergyupdate.com/csp-today/acwa-power-scales-tower-trough-design-set-record-low-csp-price> [Cited in 2017].
- [11] J. E. P. Clifford K. Ho: *Levelized Cost of Coating (LCOC) for selective absorber materials*. U.S. Department of Energy, Sandia National Laboratories, P.O.O Box5800, Albuquerque, 2014.
- [12] I. LA-CO Industries: *Product Description: Pyromark High Temperature Paint*. 2012. [Online]. Available: <http://www.tempil.com/specialty-coatings/pyromark-high-temperature-paint/> [Cited in 2017].
- [13] O.Raccurt et al.: *Study of Stability of a Selective Solar Absorber Coating under Air and High Temperature Conditions*. National Institute of Solar Energy, ARCHIMEDE Solar Energy SRL (ASE) ENEA Lungotevere Grande Ammiraglio Thaon di Revel, June 2015.
- [14] H. S. University: *GSP 216 Introduction to remote sensing*. [Online]. Available: http://gsp.humboldt.edu/olm_2015/Courses/GSP_216_Online/lesson8-1/emissivity.html
- [15] S. Ulmer: *Messung der Strahlungsflussdichte-Verteilung von punktkonzentrierenden solarthermischen Kraftwerken*. Institut für Technische Thermodynamik des DLR, Institut für Thermodynamik und Wärmetechnik der Universität Stuttgart: VDI-Verlag, 2004.

- [16] J. Ballestrin: *Direct Heat-Flux Measurement System (MDF) for Solar Central Receiver Evaluation*. Almeria: CIEMAT, April 2001.
- [17] Perkin Elmer Inc.: *LAMBDA 1050 UV/Vis Spectrophotometer*. [Online]. Available: <http://www.perkinelmer.com/es/product/lambda-1050-uv-vis-nir-spectrophotometer-l1050>
- [18] Perkin Elmer Inc.: *Frontier MIR Spectrometer*. [Online]. Available: <http://www.perkinelmer.com/es/product/frontier-mir-spectrum-10-std-l1280002>.
- [19] National. Renewable Energy Laboratory: *Solar Espectral Irradiance*. Renewable Resource Data Center, 1999. [Online]. Available: <http://rredc.nrel.gov/solar/spectra/am1.5/>
- [20] D. & Services Inc: *Portable Reflectometer D&S*. 2016. [Online]. Available: <http://www.devicesandservices.com/prod02.htm>. [Accessed in 2017].
- [21] Vallourec SAS: *VM12 Datasheet*. 2016. [Online]. Available: http://www.vallourec.com/NUCLEARPOWER/Lists/Brochures/Attachments/5/V_B01B0015B-GB.pdf
- [22] Thyssenkrupp AG: *T91 Datasheet*. [Online]. Available: http://www.s-k-h.com/media/de/Service/Werkstoffblaetter_englisch/Kesselrohre_ASTM/P91_T91_engl.pdf
- [23] Spanish Ministry of Economy: *Dish Stirling Systems*. Plataforma Solar de Almeria, [Online]. Available: <http://www.psa.es/en/instalaciones/discos/distal1.php>. [Cited in 2017].
- [24] Captec SAS: *Radiant Flux Sensors*. [Online]. Available: <https://www.captec.fr/copie-de-fluxmetre-radiatif>
- [25] J. Gustavsson: *Energy Storage Technology Comparison*. KTH School of Industrial Engineering and Management Energy Stockholm, 2016.
- [26] B. C. G. J. J. A. C. M. Köhl: *Performance and Durability Assesment*. Freiburg, Boras, Golden, Denver: Elsevier, 2004.
- [27] DLR I. f. Solarforschung: *RAISELIFE*. [Online]. Available: <https://www.raiselife.eu/activities/wp3.php>.
- [28] M. A. H. E. N. S. H. T. N. E. B. H. S. F. Trieb: *Concentrating Solar Power for the Mediterranean Region*. http://www.dlr.de/Portaldata/1/Resources/portal_news/newsarchiv2008_1/algerien_med_csp.pdf, Stuttgart, April 2005.

Appendix A:

Flux map images at 12bit depth resolution taken with the CCD method.

Images shown represent post processed final version of the flux maps
(cropped, rescaled, DNI-homogenized and represented on a 24 bit color palette)

